JOURNAL OF PETROLOGY | VOLUME 41 | NUMBER 8 | PAGES 1241–1269 | 2000

Melting Behaviour of Model Lherzolite in the System CaO–MgO–Al_2O_3–SiO_2–FeO at 0·7–2·8 GPa

GUDMUNDUR H. GUDFINNSSON* AND DEAN C. PRESNALL

MAGMALOGY LABORATORY, DEPARTMENT OF GEOSCIENCES, UNIVERSITY OF TEXAS AT DALLAS, P.O. BOX 830688, RICHARDSON, TX 75083-0688, USA

RECEIVED MARCH 11, 1999; REVISED TYPESCRIPT ACCEPTED DECEMBER 14, 1999

Fe–Mg exchange is the most important solid solution involved in partial melting of spinel lherzolite, and the system CaO–MgO–Al_2O_3–SiO_2–FeO (CMASF) is ideally suited to explore this type of exchange during mantle melting. Also, if primary mid-ocean ridge basalts are largely generated in the spinel lherzolite stability field by near-fractional fusion, then Na and other highly incompatible elements will early on become depleted in the source, and the melting behaviour of mantle lherzolite should resemble the melting behaviour of simplified lherzolite in the CMASF system. We have determined the isobarically univariant melting relations of the lherzolite phase assemblage in the CMASF system in the 0·7–2·8 GPa pressure range. Isobarically, for every 1 wt % increase in the FeO content of the melt in equilibrium with the lherzolite phase assemblage, the equilibrium temperature is lower by about 3–5°C. Relative to the solidus of model lherzolite in the CaO–MgO–Al_2O_3–SiO_2 system, melt compositions in the CMASF system are displaced slightly towards the alkalic side of the basalt tetrahedron. The transition on the solidus from spinel to plagioclase lherzolite has a positive Clapeyron slope with the spinel lherzolite assemblage on the high-temperature side, and has an almost identical position in P–T *space to the comparable transition in the CaO–MgO–Al_2O_3–SiO_2–Na_2O (CMASN) system. When the compositions of all phases are described mathematically and used to model the generation of primary basalts, temperature and melt composition changes are small as percent melting increases. More specifically, 10% melting takes place over 1·5–2°C, melt compositions are relatively insensitive to the degree of melting and bulk composition, and equilibrium and near-fractional melting yield similar melt compositions. FeO and MgO are the oxides that exhibit the greatest change in the melt with degree of melting and bulk composition. The amount of FeO decreases with increasing degree of melting, whereas the amount of MgO increases. The coefficients for Fe–Mg exchange between the coexisting crystalline phases and melt,* K_{dFe-Mg}^{xl-liq}*, show a relatively simple and predictable behaviour with pressure and temperature: the coefficients for olivine and spinel do not show significant dependence on temperature, whereas the coefficients for orthopyroxene and clinopyroxene increase with pressure and temperature. When melting of lherzolite is modeled in the CMASF system, a strong linear correlation is observed between the* mg*-number of the lherzolite and the* mg*-number of the near-solidus melts. Comparison with melting in the CMASN system indicates that Na_2O has a strong effect on lherzolite melting behaviour only at small degrees of melting.*

KEY WORDS: *CMASF; lherzolite solidus; mantle melting*

INTRODUCTION

Recent models for melt generation at mid-ocean ridges have generally assumed that partial fusion occurs by a near-fractional polybaric process in response to upwelling of the mantle (e.g. Klein & Langmuir, 1987; McKenzie & Bickle, 1988; Niu & Batiza, 1991; Kinzler & Grove, 1992*a*, 1992*b*; Langmuir *et al.*, 1992; Walter & Presnall, 1994). This process entails continuous and simultaneous change in pressure, temperature, and system composition with only small amounts of melt present at all times. To collect experimental data in natural systems relevant to the melting of the mantle that would rigorously describe such change and cover all possible melting paths would be an enormous task. To circumvent the lack of such

*Corresponding author. Present address: Nordic Volcanological Institute, Gransásvergur 50, 108 Reykjavik, Iceland. Telephone: +354-525-4489. Fax: +354-562-9767. e-mail: ghg@norvol.hi.is

data, methods have been devised that use a limited number of experimental results to describe melting as a function of pressure, temperature and bulk composition. These methods include empirical parameterization of chemical compositions of experimental melts (McKenzie & Bickle, 1988; Niu & Batiza, 1991), use of distribution coefficients to describe exchange of major elements between mantle minerals and melts (Langmuir *et al.*, 1992), thermodynamically guided description of experimentally determined phase equilibria (Kinzler & Grove, 1992*b*), and models entirely based on thermodynamic calculations (Hirschmann *et al.*, 1994; Asimow *et al.*, 1995). Obviously, these are just different ways of approximating the same physicochemical states and all methods involve parameters that depend on pressure, temperature, and composition. All of the methods must rely on a limited number of data points determined at the appropriate physical and chemical conditions. This forces employment of considerable interpolations and extrapolations in pressure, temperature, and composition space. Furthermore, melting experiments inherently reproduce isobaric batch melting and most experiments on natural peridotites involve relatively high degrees of melting because of technical limitations. Thus, most existing experimental data are not ideally suited for modeling near-fractional melting where the crystalline phases are always in equilibrium with small degree melts.

Although most recent models for mid-ocean ridge basalt (MORB) generation have been based mainly on data from experiments on natural compositions, use of phase relations from simplified systems offers some important advantages over the use of data from natural compositions. Simplified systems have the disadvantage of not having all the components in natural magmas, but modeling can be carried out more rigorously and in more detail. For example, in the present study, compositions and proportions of all phases, liquid and solid, and the changes in the compositions and proportions of the phases can be rigorously calculated for any arbitrarily chosen lherzolitic starting composition. Also, each isobar traces the compositional path of a liquidus univariant boundary line along which four crystalline phases are in equilibrium. Therefore, by selecting suitable starting mixtures, phase relations pertaining to small degree melting can be determined in runs containing large amounts of liquid, thereby avoiding problems with equilibrating and analyzing small degree melts. Phase equilibrium data from simplified systems, covering a wide range of P–T–X space and complex enough to permit detailed predictions about the melting behaviour of the mantle, are now available (e.g. Walter & Presnall, 1994) and more complex systems are within reach. Furthermore, although phase relations from systems with more than four components cannot be presented graphically, methods have been developed to deal with such systems algebraically (Presnall, 1986, 1991).

In this paper we present new experimental data from the CaO–MgO–Al_2O_3–SiO_2–FeO (CMASF) system at 0·7–2·8 GPa that are relevant to the melting behaviour of mantle lherzolite. These phase relations in the CMASF system provide an important link between phase relations in the CaO–MgO–Al_2O_3–SiO_2 (CMAS) system and natural peridotite because Fe–Mg exchange is the most important kind of solid solution occurring during melting of spinel lherzolite. Also, as the oxides CaO, MgO, Al_2O_3, SiO_2, and FeO constitute ~98–99% of the chemical composition of the mantle and ~95% of the composition of primitive basalts, our results provide a good approximation of the melting behaviour of natural lherzolite as long as very low melt percentages are avoided. Although phase relations at all melt percentages are easily determined for the simplified system, they can deviate strongly from phase relations for natural compositions at very low melt percentages because of the effect of additional components (e.g. Kushiro, 1979, fig. 6-14a).

SIMPLIFIED LHERZOLITE SYSTEMS

The simplest system that can have all the upper-mantle lherzolite phases, olivine, orthopyroxene, clinopyroxene, and one of plagioclase, spinel or garnet, in equilibrium with liquid is the quaternary CMAS system. In this system the lherzolite phase assemblage is in equilibrium with melt at isobaric invariant points. Phase relations have been determined at various pressures (e.g. Davis & Schairer, 1965; Presnall *et al.*, 1979; Fujii *et al.*, 1989; Herzberg & Gasparik, 1991; Gudfinnsson & Presnall, 1996; Milholland & Presnall, 1998; Liu & Presnall, 2000). Shi & Libourel (1991) determined the same phase relations with FeO added to the CMAS system at 0·1 MPa pressure, and we extend these data in the CMASF system to the pressure range 0·7–2·8 GPa.

In our experiments, the samples were enclosed in and equilibrated with iron capsules. Thus, iron is part of what is actually a six-phase assemblage, namely, melt, olivine, orthopyroxene, clinopyroxene, and anorthite–spinel–garnet in addition to iron. Bowen & Schairer (1935) determined phase relationships in the system MgO–FeO–SiO_2 at 0·1 MPa and found that even when in equilibrium with metallic iron, silicate liquids contain some iron in the ferric state. Observed melting behaviour in our experiments was also consistent with small amounts of ferric iron being present. Hence, in a strict sense, the phase equilibria involve six phases in the six-component system Ca–Mg–Al–Si–Fe–O, which makes the phase relations isobarically univariant. Because the activity of iron is always unity, one can project the phase equilibria from iron onto the CMASF join and treat the phase

equilibria rigorously as if the number of components were five (Presnall, 1964). Thus, at a fixed pressure and temperature, the phase relations are invariant, so that at a given pressure and temperature all the phases have a fixed composition, including ferric–ferrous ratio, irrespective of the bulk composition. As a corollary, the oxygen fugacity is buffered. It changes continuously as the phase relations change, but is fixed at a given pressure and temperature. Its exact value is not known, but is probably close to the iron–wüstite buffer, which is only slightly more reduced than the proposed redox conditions of the sub-oceanic mantle during basalt generation. On the basis of measured ferric–ferrous ratios in MORB glasses (Christie *et al.*, 1986), oxygen thermobarometry of abyssal spinel peridotites (Bryndzia *et al.*, 1989), and theoretical considerations (Ballhaus & Frost, 1994), it has been suggested that the oxygen fugacity of the sub-oceanic upper mantle averages between 1 and 2 log units below the fayalite–quartz–magnetite buffer. This is about 2–3 log units above the iron–wüstite buffer.

We have determined phase relations along isobaric univariant curves with up to 10 wt % FeO in the melt. In P–T space, these lines delineate a surface where the lherzolite phase assemblage coexists with melt. We refer to this surface as the solidus of lherzolite in the CMASF system, as it is the locus of the solidi of all lherzolite compositions in the system (here determined for solidus melts with up to 10 wt % FeO). However, this surface should not be confused with the P–T solidus curves of individual lherzolite compositions in the CMASF system that form lines on the surface, and then melt along only a part of the surface until a phase is exhausted and the phase relations are no longer tied to the surface. Compositions of all phases change continuously along the surface with discontinuities at the P–T univariant lines along which the transitions from plagioclase to spinel lherzolite and spinel to garnet lherzolite occur. These univariant lines do not refer to subsolidus transitions between different lherzolite types (which are divariant in this system) but rather to transitions in which the liquid is always present. The dataset is limited to phase relations involving all lherzolite phases so we cannot model melting beyond elimination of the first crystalline phase. This is probably not a significant liability because studies on residual abyssal peridotites (Dick *et al.*, 1984) indicate that generally none of the lherzolite phases is completely exhausted; and when clinopyroxene is missing, orthopyroxene is still saturated with the clinopyroxene component. This would be expected if the melting process is near-fractional, polybaric and isentropic, because after the elimination of clinopyroxene the melt productivity decreases significantly (Asimow *et al.*, 1997) and in most cases only a small amount of melting is likely to occur after clinopyroxene is exhausted. During isobaric melting in simple systems, the melting temperature rises rapidly after the exhaustion of a crystalline phase (Presnall, 1969) and a dramatic decrease in melt productivity occurs at a constant rate of heat input.

Table 1: Starting compositions (wt %)

	CaO	MgO	Al_2O_3	SiO_2	Fe_2O_3
CMAS-5	13·89	18·92	18·26	48·93	
CMAS-27	11·92	24·38	14·60	49·10	
CMAS-28	11·94	23·77	16·06	48·22	
CMAS-40	13·60	18·32	14·67	53·42	
CMAS-41	12·28	20·96	18·21	48·56	
CMAS-42	11·27	23·64	17·58	47·51	
CMASF-4	12·91	19·48	14·19	50·49	2·93
CMASF-6	10·57	25·44	13·95	47·79	2·24
CMASF-7	11·65	21·12	18·18	46·00	3·06
CMASF-9	11·74	21·03	15·25	46·55	5·43
CMASF-10	11·23	21·68	14·34	45·80	6·95
CMASF-11	11·93	17·47	14·53	47·29	8·78
CMASF-13	10·82	24·33	12·91	46·39	5·56

MELTING EXPERIMENTS

Starting compositions were made from calcium carbonate and high-purity oxides. Iron was added as hematite. These were carefully mixed, finely ground under ethanol, and the dried mixtures were then fired in a Pt crucible in a gas furnace at over 1500°C for at least 2 h. Iron loss to the crucible during the firing was negligible because the furnace atmosphere (air) was oxidizing. After firing, the melted mixtures were quenched in all cases to crystal-free glasses, and the glasses were then ground to a fine powder under ethanol in an agate mortar. The compositions of the starting mixtures are listed in Table 1.

All the melting experiments reported here (Table 2) were conducted at the University of Texas at Dallas using three end-loaded, solid-media, piston-cylinder presses. The pressure cell assembly is essentially the same as the one used by Presnall *et al.* (1973), with the exception that Pyrex sleeves were used instead of boron nitride sleeves and crushable alumina was used instead of mullite and fired pyrophyllite. The starting mixtures were loaded into iron capsules, of ~2·5 mm length and 2·4 mm o.d. The capsule material was ~99·5% pure iron, the main impurity being manganese. The capsules were made as two cylindrical crucibles, with one fitting tightly over the other, and during the runs the two parts welded together. Just before runs were started, the sample and assembly parts, except the Pyrex and talc sleeves, were dried at

1050°C for 1 h. Initially, the sample capsules were dried in a stream of nitrogen, yet some oxidation of the iron capsules occurred during the drying process. Subsequently, the oxidized iron on the inside of the capsules entered the samples during runs, thus causing up to 5 wt % FeO enrichment of the samples. We used this to our advantage early on by using iron-free starting compositions, which gained FeO from the capsules during the experimental runs. As the charge was equilibrated with the capsule, some iron exchange always occurred between the charge and the capsule. However, to obtain better control of the iron oxide content of the charge, we mixed a small amount of hydrogen with the nitrogen drying-gas, which successfully eliminated oxidation on the inside of the capsules during the drying process. The experimental runs were of the 'hot' piston-out type (Presnall *et al.*, 1978) with no friction correction applied. From earlier comparisons with gas-apparatus experiments the pressure uncertainty is believed to be less than $\pm 0{\cdot}05$ GPa (Presnall, 1976; Presnall *et al.*, 1978). The run temperatures were monitored using W5Re/W26Re thermocouples with no pressure correction applied to the e.m.f., and kept within 2°C of the nominal temperatures by automatic temperature controllers. Temperatures listed here are referenced to the International Temperature Scale of 1990 (ITS-90, Preston-Thomas, 1990), and are corrected to hotspot temperatures. The temperature profile for an assemblage similar to the one used here was calibrated by Walter & Presnall (1994), who estimated the thermal gradient to be 5°C across the diameter of the capsule and 10°C across the length. With one exception (Run F10·11·4, 23 h), run times were 24 or 48 h. Use of Fourier transform IR (FTIR) spectroscopy on a few of the run products indicates that the amounts of H_2O and CO_2 in the glasses are $<0{\cdot}1$ wt %.

The runs were not reversed, but on the basis of earlier studies on similar phase relations, where successful reversals were made for run durations shorter than those reported here (Presnall, 1976; Presnall *et al.*, 1978; Sen & Presnall, 1984; Liu & Presnall, 1990), we believe that equilibrium was closely approached. However, equilibrium was not perfect, as indicated by some heterogeneity in the composition of the crystalline phases, mainly in the pyroxene compositions at the lower temperatures. The consistent Fe–Mg exchange between coexisting phases also attests to a close approach to equilibrium and will be discussed in detail in a later section.

MICROPROBE ANALYSES

Longitudinal sections were made of the quenched charges, which were then mounted in epoxy, polished and inspected using a polarizing microscope. Further identification of the run products was carried out with the JEOL JXA-8600 Superprobe at the University of Texas at Dallas using backscattered electron imaging (BEI) and energy-dispersive spectrometry (EDS). In runs containing the desired phase assemblage, quantitative analyses were made of all phases (except anorthite) using wavelength-dispersive spectrometry. Both synthetic and natural minerals and glasses were used as standards. Analyses were performed with a 15 kV accelerating potential and 40 s counting time. Glass was analyzed with a 10 nA beam current, and a beam of 5 or 10 μm diameter whenever possible, but in a few cases a focused beam ($\sim$2 μm diameter) had to be used. Olivine and pyroxenes were analyzed with a 10 nA, focused beam. Spinel grains were usually very small, generally <5 μm in diameter, and to minimize the possibility of the analytical volume exceeding the size of the grains, a 5 nA beam current was used and in some cases only a very few grains could be analyzed. Analyses of olivine, pyroxenes, and spinel were reduced using the Bence–Albee correction routine (Albee & Ray, 1970), but for glass analyses the phi–rho–Z correction program (Heinrich, 1986) was used. The relative standard deviations for spot analyses of olivine, orthopyroxene, clinopyroxene, and glass were generally 1% or less for Ca, Mg, Al, and Si, but from 1% to 3% for Fe. In spinel, the same applies to Mg, Al, and Fe, but standard deviations for Ca and Si in spinel could be considerably higher, sometimes over 10%. With a few exceptions, analyses were accepted only if totals were between 99 and 101 wt %. Another criterion for accepting or rejecting analyses of the crystalline phases was their structural formulae. On the basis of six oxygen atoms, pyroxene analyses were accepted only if their cation totals were between 3·8 and 4·2; olivine and spinel analyses, calculated on the basis of four oxygen atoms, were accepted if cation totals were between 2·99 and 3·01.

PHASE COMPOSITIONS ALONG THE SOLIDUS

Run conditions and compositions of all phases except anorthite are listed in Table 2. The phase relations determined include melts with up to 10 wt % FeO at 0·7–2·8 GPa, but we find that all run products of experiments with low amounts of FeO tend to be severely heterogeneous in terms of the FeO and MgO concentrations. Therefore, only very few of the runs listed have a glass composition with <4 wt % FeO. Figure 1 shows the position of the data points on a P–T diagram. The P–T univariant liquidus boundary line, along which the transition from plagioclase to spinel lherzolite occurs, was tightly constrained by experiments at 1·0, 1·1 and 1·2 GPa, and by data from the CMAS system (Presnall

Table 2: Experimental conditions, run products, and phase compositions

		CaO		MgO		Al_2O_3		SiO_2		FeO		Total	
F7.4.2*	Glass†	14·5	(0·2)‡	10·9	(0·5)	16·1	(0·4)	49·2	(0·2)	9·10	(0·5)	99·8	(0·8)
CMASF-4	Ol	0·50	(0·1)	47·0	(0·3)			40·3	(0·2)	12·4	(0·2)	100·2	(0·3)
0·7 GPa, 1260°C, 48 h	Opx	2·91	(0·3)	31·6	(1·0)	3·60	(0·5)	55·3	(0·6)	6·05	(1·1)	99·4	(0·4)
ol+opx+cpx+an+liq	Cpx	16·2	(1·4)	21·3	(0·8)	5·15	(2·5)	52·1	(2·4)	4·99	(0·6)	99·8	(0·8)
F7.4.1	Glass	15·3	(0·2)	12·5	(0·2)	16·9	(0·2)	50·3	(0·3)	5·26	(0·3)	100·2	(0·5)
CMASF-4	Ol	0·49	(0·1)	51·0	(0·8)			41·4	(0·7)	7·14	(0·4)	100·0	(0·6)
0·7 GPa, 1270°C, 48 h	Opx	2·94	(0·6)	33·0	(1·4)	3·54	(1·0)	55·8	(0·7)	4·95	(0·7)	100·2	(0·6)
ol+opx+cpx+an+liq	Cpx	17·3	(2·1)	21·6	(2·0)	4·77	(2·1)	52·9	(1·4)	3·21	(0·4)	99·8	(0·7)
F7.C40.5	Glass	14·9	(0·1)	12·2	(0·2)	16·3	(0·4)	50·1	(0·4)	6·62	(0·3)	100·1	(0·5)
CMAS-40	Ol	0·47	(0·0)	50·4	(0·3)			41·2	(0·2)	8·67	(0·3)	100·8	(0·3)
0·7 GPa, 1275°C, 24 h	Opx	2·91	(0·4)	33·6	(0·6)	3·13	(0·4)	56·3	(0·3)	4·29	(1·0)	100·2	(0·6)
ol+opx+cpx+an+liq	Cpx	17·2	(2·5)	22·1	(1·8)	3·09	(1·4)	54·5	(0·9)	3·05	(0·9)	100·0	(0·3)
F7.C40.8	Glass	15·4	(0·1)	12·7	(0·2)	17·0	(0·3)	50·5	(0·4)	4·48	(0·3)	100·0	(0·6)
CMAS-40	Ol	0·47	(0·1)	51·8	(0·3)			41·4	(0·2)	6·33	(0·5)	100·0	(0·6)
0·7 GPa, 1285°C, 48 h	Opx	3·05	(0·4)	34·4	(0·6)	3·51	(0·4)	56·4	(0·3)	2·37	(0·5)	99·8	(0·5)
ol+opx+cpx+an+liq	Cpx	17·9	(1·6)	22·8	(1·7)	3·11	(1·1)	54·1	(0·7)	1·84	(0·6)	99·8	(0·3)
F9.11.3	Glass	14·2	(0·1)	11·5	(0·3)	16·9	(0·3)	48·6	(0·3)	8·34	(0·3)	99·5	(0·4)
CMASF-11	Ol	0·41	(0·1)	47·8	(0·6)			40·4	(0·3)	11·2	(0·3)	99·8	(0·7)
0·9 GPa, 1275°C, 24 h	Opx	2·76	(0·5)	30·5	(1·0)	5·37	(2·6)	53·9	(1·5)	6·63	(0·2)	99·2	(0·3)
ol+opx+cpx+an+liq	Cpx	12·1	(3·4)	23·7	(2·6)	5·38	(0·9)	52·4	(0·8)	5·70	(0·8)	99·3	(0·5)
F9.11.2	Glass	14·2	(0·1)	11·8	(0·2)	17·5	(0·3)	48·8	(0·4)	7·37	(0·2)	99·6	(0·6)
CMASF-11	Ol	0·59	(0·1)	48·7	(0·5)			40·9	(0·3)	10·1	(0·3)	100·2	(0·6)
0·9 GPa, 1280°C, 24 h	Opx	2·83	(0·6)	30·9	(0·3)	6·19	(1·6)	53·8	(0·8)	6·05	(0·4)	99·8	(0·5)
ol+opx+cpx+an+liq	Cpx	10·2	(1·5)	25·8	(1·1)	5·55	(0·4)	53·4	(0·5)	5·36	(0·3)	100·3	(0·5)

Table 2: continued

		CaO		MgO		Al_2O_3		SiO_2		FeO		Total	
F9.11.1	Glass	14·4	(0·2)	11·8	(0·2)	17·2	(0·3)	49·3	(0·3)	7·09	(0·3)	99·7	(0·6)
CMASF-11	Ol	0·51	(0·2)	49·5	(0·5)			41·0	(0·1)	9·63	(0·5)	100·6	(0·5)
0·9 GPa, 1285°C, 24 h	Opx	2·75	(0·4)	31·5	(0·3)	5·52	(1·2)	54·3	(0·6)	5·85	(0·2)	100·0	(0·5)
ol+opx+cpx+an+liq	Cpx	12·7	(3·3)	23·9	(2·6)	5·01	(0·7)	53·0	(1·1)	4·86	(0·6)	99·5	(0·5)
F9.9.6	Glass	15·0	(0·2)	12·9	(0·3)	17·9	(0·3)	50·1	(0·5)	4·00	(0·5)	99·9	(0·6)
CMASF-9	Ol	0·60	(0·0)	52·9	(0·4)			41·8	(0·3)	4·66	(0·1)	99·9	(0·6)
0·9 GPa, 1295°C, 48 h	Opx	2·85	(0·4)	33·2	(0·9)	5·41	(1·7)	54·8	(1·2)	3·33	(0·8)	99·5	(0·7)
ol+opx+cpx+an+liq	Cpx	15·8	(3·0)	23·1	(2·6)	5·62	(1·4)	52·7	(1·2)	2·21	(0·6)	99·3	(0·7)
F10.11.4	Glass	13·7	(0·2)	10·9	(0·2)	17·5	(0·4)	48·0	(0·5)	9·51	(0·3)	99·7	(0·7)
CMASF-11	Ol	0·37	(0·1)	46·8	(0·4)			40·0	(0·3)	12·8	(0·3)	99·9	(0·5)
1·0 GPa, 1281°C, 23 h	Opx	2·87	(0·4)	30·0	(0·6)	5·97	(0·9)	54·2	(0·6)	7·76	(0·4)	100·9	(0·5)
ol+opx+cpx+an+liq	Cpx	13·9	(3·1)	21·9	(2·5)	6·09	(2·1)	52·8	(1·2)	6·22	(0·9)	100·9	(0·9)
F11.11.2	Glass	14·3	(0·3)	11·6	(0·6)	18·7	(0·2)	47·6	(0·5)	7·80	(0·5)	100·0	(0·9)
CMASF-11	Ol	0·54	(0·1)	48·2	(0·7)			40·6	(0·2)	10·6	(0·8)	99·9	(0·5)
1·1 GPa, 1300°C, 24 h	Opx	2·68	(0·5)	30·9	(1·0)	6·19	(2·1)	53·7	(1·2)	6·30	(0·6)	99·8	(0·6)
ol+opx+cpx+an+liq	Cpx	15·3	(2·3)	21·2	(1·9)	7·27	(1·5)	51·4	(1·1)	4·73	(0·7)	99·9	(0·7)
F11.C41.7	Glass	14·4	(0·2)	12·7	(0·2)	18·9	(0·4)	47·7	(0·3)	6·22	(0·2)	99·9	(0·8)
CMAS-41	Ol	0·49	(0·1)	50·5	(0·3)			41·1	(0·4)	8·11	(0·4)	100·2	(0·6)
1·1 GPa, 1310°C, 24 h	Opx	2·68	(0·8)	32·7	(0·7)	8·12	(1·1)	54·2	(0·6)	2·89	(1·3)	100·5	(0·4)
ol+opx+cpx+an+liq	Cpx	17·5	(1·1)	20·3	(1·3)	9·41	(1·3)	50·8	(0·7)	2·67	(1·1)	100·7	(0·4)
F11.7.2	Glass	14·6	(0·2)	13·1	(0·2)	19·2	(0·3)	47·9	(0·3)	5·08	(0·2)	99·9	(0·3)
CMASF-7	Ol	0·43	(0·1)	51·6	(0·6)			41·4	(0·4)	6·16	(0·3)	99·6	(0·6)
1·1 GPa, 1320°C, 48 h	Opx	2·38	(0·2)	32·5	(0·4)	8·38	(1·5)	53·3	(1·2)	3·55	(0·2)	100·1	(0·7)
ol+opx+cpx+sp+liq	Cpx	16·7	(2·1)	21·2	(1·2)	8·26	(1·3)	50·9	(1·0)	2·56	(0·5)	99·6	(0·6)
	Sp	0·20	(0·1)	25·7	(0·3)	69·5	(0·8)	0·43	(0·1)	4·59	(0·5)	100·4	(0·8)

		CaO		MgO		Al_2O_3		SiO_2		FeO		Total	
F12.11.4	Glass	13·6	(0·2)	11·4	(0·4)	18·4	(0·4)	46·4	(0·5)	9·63	(0·4)	99·4	(0·7)
CMASF-11	Ol	0·57	(0·1)	46·6	(0·4)			40·4	(0·5)	12·6	(0·3)	100·2	(0·8)
1·2 GPa, 1318°C, 24 h	Opx	2·64	(0·3)	30·2	(1·0)	6·73	(2·6)	53·7	(1·5)	7·19	(0·4)	100·5	(0·6)
ol+opx+cpx+an+sp+liq	Cpx	14·4	(1·5)	21·0	(1·6)	8·02	(2·0)	51·2	(1·3)	5·67	(0·6)	100·2	(0·6)
	Sp (5)	0·31	(0·1)	22·5	(0·3)	67·9	(0·8)	0·91	(0·2)	8·72	(0·5)	100·3	(0·8)
F12.9.4	Glass	14·1	(0·1)	12·6	(0·2)	18·8	(0·4)	47·3	(0·6)	7·44	(0·2)	100·2	(0·9)
CMASF-9	Ol	0·53	(0·1)	49·3	(0·5)			40·9	(0·7)	9·57	(0·2)	100·3	(0·9)
1·2 GPa, 1325°C, 24 h	Opx	2·43	(0·2)	30·5	(0·9)	8·27	(2·5)	52·5	(1·3)	6·19	(0·3)	99·9	(0·5)
ol+opx+cpx+sp+liq	Cpx	16·4	(0·8)	20·1	(0·9)	8·61	(1·2)	50·2	(1·2)	4·07	(0·2)	99·4	(0·4)
	Sp (3)	0·37	(0·4)	24·5	(1·2)	68·0	(2·0)	1·34	(0·7)	6·66	(0·8)	100·8	(0·5)
F14.11.4	Glass	14·0	(0·2)	11·7	(0·9)	18·8	(0·8)	46·1	(0·6)	8·90	(0·4)	99·5	(0·7)
CMASF-11	Ol	0·53	(0·0)	47·7	(0·4)			40·5	(0·2)	11·1	(0·3)	99·9	(0·8)
1·4 GPa, 1345°C, 24 h	Opx	2·55	(0·3)	29·8	(0·7)	8·04	(1·5)	53·1	(1·2)	6·59	(0·4)	100·1	(0·5)
ol+opx+cpx+sp+liq	Cpx	13·8	(1·8)	21·5	(1·4)	8·13	(1·5)	50·8	(1·0)	5·32	(0·5)	99·6	(0·5)
	Sp (5)	0·22	(0·1)	23·5	(0·3)	68·4	(0·8)	0·83	(0·1)	7·77	(0·2)	100·7	(0·6)
F14.C5.8	Glass	14·1	(0·1)	13·6	(0·2)	18·4	(0·3)	46·8	(0·3)	7·37	(0·3)	100·3	(0·6)
CMAS-5	Ol	0·37	(0·1)	50·1	(0·4)			41·0	(0·2)	8·67	(0·3)	100·2	(0·6)
1·4 GPa, 1360°C, 24 h	Opx	2·48	(0·2)	30·7	(0·9)	7·97	(2·0)	53·4	(1·3)	5·11	(0·4)	99·7	(0·4)
ol+opx+cpx+sp+liq	Cpx	16·7	(1·2)	19·6	(1·3)	9·48	(0·6)	50·4	(0·6)	3·48	(0·7)	99·6	(0·5)
	Sp	0·16	(0·1)	24·3	(0·3)	68·7	(0·7)	0·23	(0·1)	6·47	(0·3)	99·9	(0·8)
F14.9.8	Glass	14·8	(0·2)	14·3	(0·4)	19·4	(0·4)	47·8	(0·2)	3·62	(0·3)	100·0	(0·8)
CMASF-9	Ol	0·59	(0·1)	53·2	(0·4)			42·0	(0·1)	4·49	(0·3)	100·3	(0·5)
1·4 GPa, 1370°C, 24 h	Opx	2·85	(1·1)	32·3	(1·3)	8·12	(2·0)	53·6	(1·5)	2·86	(0·3)	99·8	(0·7)
ol+opx+cpx+sp+liq	Cpx	15·9	(1·9)	21·8	(1·5)	8·81	(1·2)	51·1	(1·0)	2·15	(0·6)	99·7	(0·5)
	Sp	0·49	(0·1)	25·6	(0·2)	69·0	(0·6)	1·45	(0·3)	3·13	(0·5)	99·6	(0·7)

Table 2: continued

		CaO		MgO		Al_2O_3		SiO_2		FeO		Total	
F17.C5.4	Glass	13·8	(0·1)	14·8	(0·2)	18·0	(0·3)	46·6	(0·4)	6·91	(0·3)	100·1	(0·6)
CMAS-5	Ol	0·51	(0·0)	50·3	(0·3)			40·8	(0·3)	7·90	(0·3)	99·5	(0·6)
1·7 GPa, 1395°C, 24 h	Opx	2·88	(1·3)	30·9	(2·4)	8·84	(1·7)	52·8	(1·0)	4·41	(0·8)	99·8	(0·7)
ol+opx+cpx+sp+liq	Cpx	15·2	(0·5)	21·3	(0·8)	9·50	(0·9)	51·2	(0·7)	3·27	(0·4)	100·4	(0·5)
	Sp	0·16	(0·1)	24·5	(0·2)	69·0	(0·4)	0·28	(0·1)	5·41	(0·3)	99·3	(0·3)
F17.C42.1	Glass	14·5	(0·1)	15·8	(0·3)	18·7	(0·3)	47·5	(0·3)	4·10	(0·2)	100·7	(0·5)
CMAS-42	Ol	0·48	(0·0)	53·3	(0·4)			41·8	(0·3)	4·66	(0·2)	100·2	(0·5)
1·7 GPa, 1405°C, 24 h	Opx	2·49	(0·2)	32·4	(0·9)	9·00	(1·9)	53·5	(1·1)	2·97	(0·2)	100·4	(0·8)
ol+opx+cpx+sp+liq	Cpx	15·4	(0·8)	22·0	(0·7)	9·59	(0·9)	51·2	(0·5)	2·13	(0·2)	100·4	(0·2)
	Sp (5)	0·22	(0·2)	26·6	(0·3)	70·0	(0·6)	0·61	(0·6)	3·10	(0·2)	100·5	(0·3)
F20.C27.3	Glass	12·8	(0·2)	14·5	(0·2)	16·6	(0·4)	45·5	(0·2)	10·2	(0·3)	99·5	(0·5)
CMAS-27	Ol	0·49	(0·0)	47·3	(0·5)			40·3	(0·2)	11·6	(0·6)	99·7	(0·9)
2·0 GPa, 1425°C, 24 h	Opx	2·60	(0·1)	29·4	(0·4)	8·88	(1·0)	52·0	(0·6)	6·54	(0·2)	99·5	(0·5)
ol+opx+cpx+sp+liq	Cpx	12·5	(0·7)	21·3	(0·6)	9·41	(0·7)	50·4	(0·5)	5·66	(0·3)	99·3	(0·3)
	Sp	0·19	(0·1)	23·2	(0·5)	67·6	(1·4)	0·41	(0·2)	7·74	(0·4)	99·1	(0·7)
F20.C28.3	Glass	13·9	(0·2)	16·7	(0·6)	17·7	(0·4)	46·9	(0·2)	4·39	(0·1)	99·6	(0·5)
CMAS-28	Ol	0·46	(0·0)	53·1	(0·7)			41·9	(0·2)	4·69	(0·2)	100·1	(0·8)
2·0 GPa, 1450°C, 48 h	Opx	2·51	(0·1)	32·3	(0·5)	9·91	(1·3)	53·2	(0·6)	2·79	(0·2)	100·7	(0·4)
ol+opx+cpx+sp+liq	Cpx	14·0	(1·0)	22·8	(0·9)	10·4	(1·0)	50·9	(0·6)	2·17	(0·2)	100·2	(0·4)
	Sp	0·15	(0·1)	26·5	(0·4)	70·1	(0·6)	0·51	(0·3)	3·10	(0·2)	100·3	(0·7)
F23.10.13	Quench	13·3	(0·9)	17·4	(2·4)	17·0	(0·6)	46·6	(0·4)	5·48	(1·4)	99·7	(0·7)
CMASF-10	Ol	0·54	(0·1)	52·3	(0·5)			41·4	(0·4)	5·44	(0·2)	99·7	(0·6)
2·3 GPa, 1475°C, 24 h	Opx	2·60	(0·1)	31·5	(0·6)	9·44	(1·7)	53·0	(1·1)	3·57	(0·4)	100·1	(0·6)
ol+opx+cpx+sp+liq	Cpx	12·9	(0·9)	23·5	(0·6)	9·88	(0·4)	50·8	(0·4)	2·92	(0·4)	100·0	(0·5)
	Sp	0·41	(0·1)	25·9	(0·3)	68·6	(0·4)	1·24	(0·1)	3·58	(0·1)	99·7	(0·7)

		CaO		MgO		Al_2O_3		SiO_2		FeO		Total	
F27.C27.2	Quench	13·4	(0·6)	17·3	(2·1)	16·8	(0·8)	46·1	(0·5)	6·47	(1·2)	100·1	(0·9)
CMAS-27	Ol	0·53	(0·1)	51·4	(0·5)			41·5	(0·3)	7·00	(0·3)	100·5	(0·6)
2·7 GPa, 1510°C, 24 h	Opx	2·72	(0·1)	31·1	(0·3)	9·27	(0·9)	52·4	(0·5)	4·00	(0·2)	99·4	(0·5)
ol + opx + cpx + sp + liq	Cpx	12·2	(1·0)	23·2	(0·8)	10·1	(0·9)	51·1	(0·6)	3·44	(0·4)	100·1	(0·3)
	Sp	0·10	(0·1)	25·5	(0·3)	69·2	(0·7)	0·49	(0·1)	4·88	(0·4)	100·2	(0·9)
F27.6.11	Quench	13·6	(0·2)	19·5	(0·5)	17·4	(0·2)	47·0	(0·5)	2·22	(0·5)	99·6	(0·8)
CMASF-6	Ol	0·55	(0·1)	55·0	(0·3)			42·2	(0·3)	1·86	(0·2)	99·5	(0·5)
2·7 GPa, 1530°C, 24 h	Opx	2·64	(0·2)	33·0	(0·6)	9·50	(0·9)	53·1	(0·7)	1·15	(0·2)	99·4	(0·5)
ol + opx + cpx + sp + liq	Cpx	13·0	(0·5)	24·4	(0·4)	9·73	(0·4)	51·3	(0·2)	0·95	(0·1)	99·5	(0·5)
	Sp (5)	0·34	(0·2)	27·9	(0·9)	69·9	(0·6)	1·27	(0·4)	1·31	(0·2)	100·7	(0·8)
F28.13.1	Quench	12·7	(0·9)	18·7	(1·2)	16·5	(0·3)	46·5	(0·6)	4·67	(0·9)	99·0	(0·6)
CMASF-13	Ol	0·38	(0·0)	53·0	(0·4)			41·6	(0·3)	4·57	(0·2)	99·6	(0·6)
2·8 GPa, 1530°C, 24 h	Opx	2·63	(0·1)	32·0	(0·7)	9·21	(1·9)	53·7	(1·1)	3·05	(0·2)	100·6	(0·5)
ol + opx + cpx + sp + liq	Cpx	11·5	(1·1)	24·5	(1·0)	9·80	(0·6)	51·8	(0·5)	2·65	(0·3)	100·2	(0·7)
	Sp	0·12	(0·0)	26·1	(0·3)	70·4	(0·8)	0·54	(0·0)	2·92	(0·3)	100·1	(0·9)

*Information listed about runs: run number, starting mixture, pressure, temperature, duration of run, and phase assemblage. ol, olivine; opx, orthopyroxene; cpx, clinopyroxene; an, anorthite; sp, spinel; liq, liquid.
†Ten spot analyses were made of each phase, unless otherwise indicated.
‡Mean and 2 SD for microprobe analyses, wt %.

et al., 1979) where the P–T invariant reaction involving forsterite, enstatite, diopside, anorthite, spinel and melt occurs at 0·93 GPa, 1300°C. One of the 1·2 GPa runs from the CMASF dataset contains the six-phase assemblage and thus lies on the transition line. The linear equation $T(°C) = 59·3P(GPa) + 1247$ passes through the 0·93 and 1·2 GPa points and describes the position of the transition in P–T space. Although the melting temperature of pure Fe metal is ~1640°C at 3·0 GPa (Liu & Bassett, 1975), we find that experiments approaching 3·0 GPa, at temperatures higher than 1550°C, frequently fail as a result of melting of the Fe capsules, which is probably because of the presence of small amounts of impurities in the metal. This makes it impossible to perform experiments using Fe capsules much beyond the spinel to garnet lherzolite transition. In spite of these problems, use of the transition from spinel to garnet lherzolite on the solidus of model lherzolite in the CMAS system at 3·0 GPa, 1568°C (Milholland & Presnall, 1998), and bracketing points in the spinel field at 2·7 and 2·8 GPa and in the garnet field at 2·9 GPa yields an approximate equation for this transition of $T(°C) = 283P(GPa) + 726$.

Mathematical description of phase compositions

As previously explained, our dataset has the advantage of being continuous in pressure, temperature and composition space, but because it involves five components, it cannot be presented graphically as a phase diagram. Instead, we have described the phase compositions mathematically. For the mathematical description, in addition to our own data, we include data from Shi & Libourel (1991), who determined the isobaric divariant liquidus phase relations in the CMASF system involving olivine, augite and anorthite in equilibrium with liquid at 0·1 MPa. This divariant surface is bounded on one side by an isobaric univariant curve, where at low FeO contents the phase assemblage is joined by orthopyroxene and at higher FeO contents by pigeonite. The univariant data were included in the description of the phase compositions. It should be noted, however, that there is a slight loss of precision for orthopyroxene compositions at low pressures because at relatively high FeO contents we interpolate from low-CaO clinopyroxene compositions to orthopyroxene compositions. As the univariant liquidus phase relations in the CMAS system involving the lherzolite phase assemblage border the divariant phase relations in the CMASF system involving the same phase assemblage, we have included data on liquidus phase relations of model lherzolite in the CMAS system from experiments conducted by Presnall *et al.* (1979) and by Milholland & Presnall (1998). The run products of Presnall *et al.* (1979) were reanalyzed by Walter & Presnall (1994) and their analyses are included here along with data on the same phase relations at 2·4–2·8 GPa from Gudfinnsson & Presnall (1996). For reasons explained below, three of our 0·9 GPa clinopyroxene compositions at 1275°C, 1280°C and 1285°C were not used in the mathematical description.

To describe the compositional variation of the melt and the crystalline phase, we have elected to describe each oxide in every phase as a function of pressure and temperature in a way similar to that done by Walter & Presnall (1994). Employing least-squares multiple linear regression, a first-degree polynomial expression with a cross-product term added was fitted to the experimental data. The expression has the form

$$X_j^i = \alpha + 10\beta P + 10\chi P(T/10\,000) + \delta P(T/10\,000)$$

where X_j^i is the concentration of oxide i in phase j in weight percent, P is the pressure in GPa, T is the temperature in °C, and α, β, χ, and δ are regression coefficients. Because of the breaks in compositional trends at the transitions from plagioclase to spinel lherzolite and spinel to garnet lherzolite, the phase compositions cannot adequately be described by one set of equations. Therefore, we divide the lherzolite solidus into regions and treat each region individually. As the curvature of the compositional trends changes considerably above ~0·9 GPa in the plagioclase lherzolite field as the plagioclase to spinel lherzolite transition is approached, the plagioclase lherzolite stability field is divided into two regions, separated at the 0·9 GPa isobar. The spinel lherzolite field is treated as one region. The resulting regression coefficients, α, β, χ, and δ, and the coefficients of multiple correlation for the fits are listed in Table 3. An analysis of variance was performed on the regression data, and the F-test reveals that the regressions are in most cases significant at the 5% level and in most of these cases also at the 1% level. The fits that are not significant at the 5% level are for oxides in small amounts, CaO in olivine and CaO and SiO_2 in spinel, and for oxides that vary little compared with their analytical uncertainty, for example, SiO_2 in pyroxenes in the spinel lherzolite region. Second-degree polynomial fits and first-degree polynomial fits without the cross-product term were also tried. Analysis of variance reveals that for 24 of 62 cases, second-degree polynomial equations lead to improvement over first-degree equations at the 5% significance level, whereas in 25 of 62 cases, first-degree equations with the cross-product term added lead to improvements over first-degree equations. Only in six of 62 cases do second-degree equations lead to improvement over first-degree equations with the cross-product term added. Simple equations have the advantage of allowing slight extrapolations beyond the limits of the dataset without the possibility of excessive deviations from the trend of the

*Table 3: Regression coefficients for polynomial fits to phase compositions**

	α	β	χ	δ	σ†	*R*‡
Region 1. Plagioclase lherzolite stability field, ≤0·9 GPa						
Glass, n§ = 14						
CaO	−27·5382	0·588606	−6·78172	348·044	0·15	0·99
MgO	−87·1794	−3·40248	23·5184	802·006	0·43	0·97
Al_2O_3	−54·5295	−6·00355	46·4638	565·249	0·51	0·96
SiO_2	−29·8238	−0·880371	−0·960377	685·295	0·27	0·96
FeO	299·054	9·69703	−62·2367	−2400·45	1·1	0·97
Olivine, n = *14*						
CaO	3·66190	0·185442	−1·21658	−26·7768	0·06	0·57
MgO	−349·750	−5·09679	22·5555	3268·32	1·1	0·98
SiO_2	−41·8390	−1·58632	8·77451	677·672	0·26	0·98
FeO	487·922	6·50459	−30·1682	−3919·15	1·3	0·99
Orthopyroxene, n = *14*						
CaO	43·2528	−2·59812	20·0333	−314·001	0·13	0·99
MgO	−203·396	3·86860	−40·3380	1926·43	0·62	0·99
Al_2O_3	11·0660	−8·41355	70·2728	−85·1244	0·46	0·99
SiO_2	−18·9492	4·15808	−38·1357	624·764	0·31	0·99
FeO	268·054	2·98575	−11·8341	−2152·31	0·83	0·98
Clinopyroxene, n = *11*						
CaO	−11·8269	−10·1897	75·9086	255·982	0·57	0·80
MgO	−79·1277	9·58201	−78·2602	816·703	0·48	0·96
Al_2O_3	−1·36929	−8·89729	72·5120	26·2700	0·78	0·92
SiO_2	13·0637	5·28604	−45·1147	341·910	0·54	0·84
FeO	179·398	4·22923	−25·1250	−1441·99	0·46	0·99

data. At the same time, statistically good fits are desirable. To balance these requirements, it was decided to adopt the first-degree fits with a cross-product term added.

As we will elucidate in a later section, melting of the lherzolite assemblage in the CMASF system occurs over a small temperature interval in comparison with the temperature uncertainty of the experiments (±10°C), such that isobarically 10% melting is attained by raising the temperature 1·5–2°C. The regression fits to the experimental data tend to average out the uncertainty in the experimental temperatures, and so, when displaying the compositional trends in the CMASF system, they can be more clearly demonstrated, as we will do in the following sections, by deriving them from the polynomial equations rather than directly using the experimental data points.

In the following discussion, we describe variations in the Fe–Mg exchange coefficients between minerals and melt as a function of pressure. It should be noted, however, that because of the low variance of the phase relations and the melting characteristics, there is a very strong correlation between pressure, temperature, and composition, and hence the choice of pressure as the independent variable is largely arbitrary. The observation that two-component distribution coefficients tend to be relatively insensitive to changes in temperature and melt composition (Takahashi & Irvine, 1981), is some justification for this choice.

Melt compositions

In Fig. 1, in addition to displaying the experimental points, we show the lherzolite solidus in the CMAS system and isopleths of FeO content in melts that coexist with a lherzolite phase assemblage in the CMASF system. Temperature depression of the solidus caused by the addition of FeO to the CMAS system is in the range of 3–5°C for every 1 wt % increase in the FeO content of the melt. Because the FeO content of anorthite is negligible and spinel is an FeO-rich phase, it was expected that addition of FeO would stabilize the plagioclase to spinel lherzolite transition reaction down-temperature and down-pressure relative to FeO-free systems, but we

Table 3: continued

	α	β	χ	δ	σ†	*R*‡
Region 2. Plagioclase lherzolite stability field, >0·9 GPa						
Glass, n = *9*						
CaO	−148·338	11·9490	−96·2159	1296·68	0·10	0·95
MgO	−410·100	29·5686	−236·611	3345·79	0·32	0·91
Al_2O_3	−529·574	45·6590	−353·390	4241·79	0·36	0·88
SiO_2	−149·516	13·9260	−117·390	1629·04	0·09	0·99
FeO	1335·21	−100·853	801·682	−10495·5	0·62	0·95
Olivine, n = *9*						
CaO	44·1872	−4·50858	34·6352	−335·995	0·07	0·43
MgO	−1462·87	114·857	−912·391	11943·8	0·63	0·96
SiO_2	−227·827	18·0757	−145·982	2140·78	0·16	0·96
FeO	1747·55	−128·520	1024·47	−13756·5	0·73	0·96
Orthopyroxene, n = *9*						
CaO	66·1105	−4·45140	35·1036	−497·488	0·11	0·67
MgO	−702·777	53·8522	−429·468	5811·86	0·39	0·95
Al_2O_3	−250·033	20·7477	−159·265	1971·76	0·52	0·66
SiO_2	−80·8532	9·18027	−75·7122	1091·50	0·12	0·95
FeO	1068·55	−79·4535	630·277	−8385·08	0·79	0·90
Clinopyroxene, n = 6						
CaO	−301·303	17·8673	−150·163	2575·30	0·70	0·85
MgO	4·24201	0·168866	−4·18515	159·417	0·60	0·44
Al_2O_3	−91·2157	4·17075	−30·4557	742·222	0·56	0·82
SiO_2	72·5691	−0·675616	2·45293	−133·159	0·35	0·78
FeO	415·707	−21·5313	182·351	−3343·78	0·30	0·96

observe that in P–T space the transition line extends instead to higher temperatures and pressures and nearly overlaps the corresponding line in the FeO-free CaO–MgO–Al_2O_3–SiO_2–Na_2O (CMASN) system (Walter & Presnall, 1994). This can be explained by the fact that the transition reaction from spinel to plagioclase lherzolite consumes only small amounts of spinel (see a later section), and, consequently, changes in spinel composition have little effect on the position of the transition line in P–T space. The spinel to garnet lherzolite transition, however, is stabilized to lower temperatures and pressures compared with the CMASN system (Fig. 1).

Figure 2a and b depicts normative compositions of melts in two ternary projections as yielded by the polynomial equations. When compared with identical plots for melts in the CMASN system (Walter & Presnall, 1994), it is obvious that addition of FeO to the CMAS system causes much less shift in phase boundaries than does addition of Na_2O. With the addition of modest amounts of Na_2O, melt compositions shift considerably to the alkalic side of the Ol–Cpx–An–Qz quaternary, such that for certain parts of the spinel field in the CMASN system, melts with only 2 wt % or less Na_2O are Ne-normative. The changes in the CMASF system are more prominent in the plagioclase field than in the spinel field, but overall the trends are slightly toward the alkalic side of the phase diagram with increasing FeO content. This kind of quaternary projection, however, is not ideally suited for demonstrating trends in the CMASF system, because it combines FeO and MgO as one component, and thus can conceal information about the different effects of FeO and MgO on the phase equilibria. Figure 3, which depicts the relation between the cation fraction of Mg and Fe in the melt at two pressures, shows that as the amount of Fe increases, so does the sum of Mg and Fe. In other words, at lower temperatures the melts become less magnesian, but, at the same time, more ferro-magnesian. Comparable change in melt composition occurs at 0·1 MPa along the univariant line with olivine and pyroxene in equilibrium with liquid in the MgO–FeO–SiO_2 system (Fig. 3) (Bowen & Schairer, 1935).

Table 3: continued

	α	β	χ	δ	σ†	*R*‡
Region 3. Spinel lherzolite stability field						
Glass, n = *21*						
CaO	−6·36465	−0·954415	3·78162	196·330	0·23	0·91
MgO	−103·617	−3·08617	12·9781	1001·72	0·56	0·97
Al_2O_3	7·96396	−1·35344	6·19282	130·980	0·30	0·96
SiO_2	9·46617	−2·59510	12·1440	375·917	0·37	0·96
FeO	192·643	7·98903	−35·0873	−1705·75	1·1	0·96
Olivine, n = *21*						
CaO	4·11727	0·156093	−0·647606	−33·8757	0·05	0·77
MgO	−136·167	−7·14112	30·2421	1691·97	1·3	0·95
SiO_2	−0·108175	−1·72280	7·61257	375·285	0·24	0·96
FeO	240·164	8·94370	−38·1179	−2102·67	1·5	0·96
Orthopyroxene, n = *21*						
CaO	4·59534	0·265463	−1·26701	−24·9262	0·10	0·77
MgO	−52·2455	−4·51162	20·8779	790·249	0·73	0·93
Al_2O_3	−30·1831	0·706261	−5·83201	291·353	0·34	0·91
SiO_2	39·7779	−1·75551	9·04165	154·278	0·33	0·83
FeO	137·877	5·30062	−22·8620	−1209·56	0·88	0·95
Clinopyroxene, n = *21*						
CaO	−57·0852	−3·55011	14·0700	706·210	0·77	0·95
MgO	18·1584	−0·876799	6·42605	20·7606	0·53	0·92
Al_2O_3	−39·1868	0·650272	−6·38046	376·643	0·29	0·87
SiO_2	55·5446	−0·637149	4·16836	−26·9884	0·20	0·74
FeO	122·746	4·41814	−18·2944	−1078·18	0·69	0·96
Spinel, n = *21*						
CaO	3·70973	0·181675	−0·846347	−32·5240	0·09	0·56
MgO	−80·3873	−3·80882	15·9297	945·268	0·69	0·96
Al_2O_3	−5·74269	−2·84750	12·0344	675·726	0·61	0·90
SiO_2	11·4694	0·409495	−1·71029	−97·8887	0·29	0·43
FeO	168·476	6·06284	−25·5356	−1470·55	1·1	0·95

*Regression coefficients for first-order polynomial equation of the form $X_j^i = \alpha + 10\beta P + 10\chi P(T/10\,000) + \delta(T/10\,000)$ where X_j^i is weight percent oxide *i* in phase *j*, *P* is pressure in GPa and *T* is temperature in °C.
†Average difference between observed and regressed values.
‡Coefficient of multiple correlation.
§Number of data points used in the regression.

Olivine

The olivine compositions in this study are forsterite–fayalite solid solutions, in most cases containing 0·4–0·8 mol % larnite component (Ca_2SiO_4). Analyses of Al_2O_3 in olivine were generally not acquired, but a few analyses that included Al_2O_3 yielded amounts on the order of 0·1–0·2 wt %. The distribution coefficient for Fe^{2+}–Mg exchange between olivine and liquid, $K_{d\,Fe^{2+}-Mg}^{ol-liq}$, has been observed to be relatively insensitive to temperature and composition, but some studies indicate that it increases slightly with pressure (Ulmer, 1989), whereas Kushiro & Walter (1998) proposed that melt composition has more effect than pressure or temperature. Most studies indicate that $K_{d\,Fe^{2+}-Mg}^{ol-liq}$ is close to 0·30 at 0·1 MPa (Roeder & Emslie, 1970; Takahashi & Kushiro, 1983; Ulmer, 1989), but between 0·35 and 0·40 at 3·0 GPa (Takahashi & Kushiro, 1983; Ulmer, 1989). The $K_{d\,Fe-Mg}^{ol-liq}$ values determined from our data are in good agreement with the 0·1 MPa values of Shi & Libourel (1991) (Fig. 4a), which are slightly higher than 0·30. The CMASF data seem to indicate a slight increase in the Fe–Mg exchange coefficient with pressure (Fig. 4a).

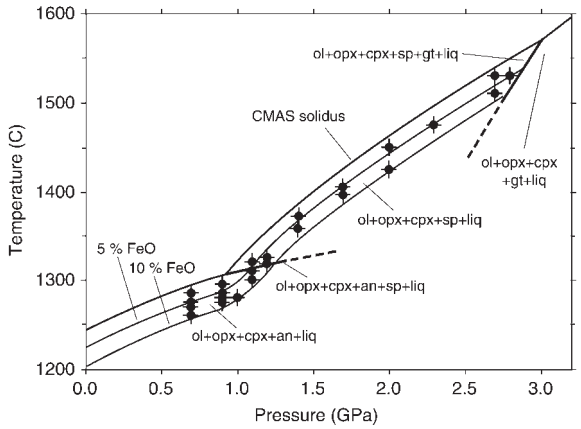

Fig. 1. Pressure–temperature diagram showing lines of equal FeO content (in wt %) of liquids. The solidus of model lherzolite in the CMAS system (0% FeO) is also shown [from Presnall *et al.* (1979) (0·1 MPa–2·0 GPa); Gudfinnsson & Presnall (1996) (2·4–3·4 GPa); Milholland & Presnall (1998) (3·0 GPa)]. Univariant lines defining the transitions on the solidus (in the presence of liquid) from garnet to spinel lherzolite and spinel to plagioclase lherzolite are shown as bold lines. ●, Experimental data points with corresponding error bars.

However, a least-squares multiple linear regression using a non-thermodynamically based polynomial equation was performed, with pressure and temperature as the independent variables and $K_{d\,Fe-Mg}^{ol-liq}$ as the dependent variable, and neither first- nor second-degree fits turned out to be significant at the 5% significance level. This does not necessarily mean that the data are highly scattered, but seems to indicate that the coefficient is insensitive to changes in pressure and temperature. The average of the exchange coefficients, including the points of Shi & Libourel (1991), is 0·327 $\pm$ 0·016. When compared with the trends of Takahashi & Kushiro (1983) and Ulmer (1989) it can be seen that their lines are within the 1σ error bars of our data points (Fig. 4a). Kushiro & Walter (1998) expressed the value of the exchange coefficient as a function of degree of polymerization of the melt, NBO/T (the number of non-bridging oxygen atoms per number of tetrahedrally coordinated cations) (Mysen *et al.*, 1982), and when their equation is used to calculate the exchange coefficient from glass compositions in the CMASF experiments at 0·7–2·8 GPa, it yields $K_{d\,Fe-Mg}^{ol-liq}$ of about 0·31–0·33, generally increasing with pressure. This is in excellent agreement with our observed values.

Pyroxene

In agreement with the common observation that pyroxenes equilibrate very slowly at low to moderate magmatic temperatures (e.g. Takahashi & Kushiro, 1983; Walter & Presnall, 1994), we find that the pyroxenes are the most heterogeneous of the phases produced in the CMASF experiments. This is evident from the Fe–Mg exchange between melt and both orthopyroxene (Fig. 4b) and clinopyroxene (Fig. 4c). Yet there are clear trends of increasing $K_{d\,Fe-Mg}^{px-liq}$ with increasing pressure that are in good agreement with the 0·1 MPa data of Shi & Libourel (1991). However, probably because of deviation from equilibrium, some of the lower-temperature runs have $K_{d\,Fe-Mg}^{px-liq}$ values that are off the main trends of the data.

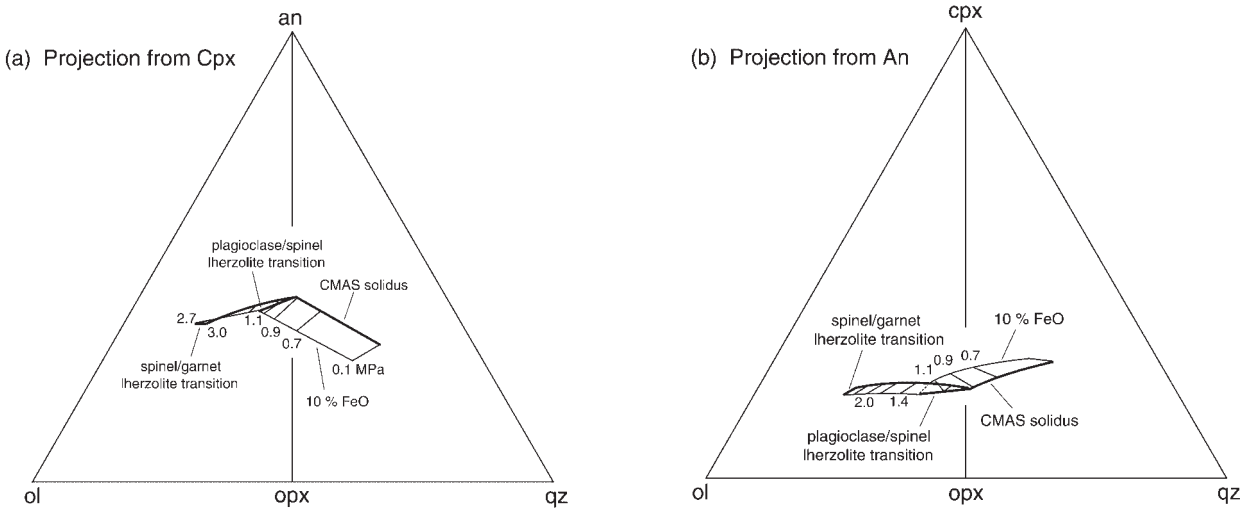

Fig. 2. Molecular CIPW normative diagram depicting melt compositions at the CMASF lherzolite solidus. The bold lines indicate (1) the garnet to spinel lherzolite and the spinel to plagioclase lherzolite transitions in the presence of liquid and (2) the CMAS solidus [0·1 MPa–2·0 GPa and 3·0 GPa runs reanalyzed by Walter & Presnall (1994); 2·4–2·8 GPa data from Gudfinnsson & Presnall (1996)]. Numbers next to the isobars indicate the pressures (in GPa). (a) Projection from Cpx. (b) Projection from An. Ol, Mg_2SiO_4 + Fe_2SiO_4; Qz, SiO_2; An, $CaAl_2Si_2O_8$; Cpx, $CaMgSi_2O_6$ + $CaFeSi_2O_6$.

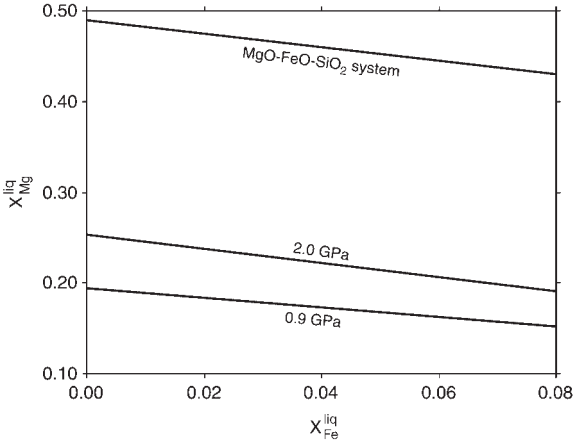

Fig. 3. Variation diagram showing cation fraction of Mg in the melt vs cation fraction of Fe in the melt at the CMASF solidus at 0·9 and 2·0 GPa, and along the 0·1 MPa univariant line with olivine and orthopyroxene in equilibrium with liquid in the MgO–FeO–SiO_2 system (Bowen & Schairer, 1935). In all cases as the fraction of Fe increases in the melt with falling temperature the fraction of Mg decreases, but by a smaller amount.

Nevertheless, analysis of variance indicates that the least-squares linear regression fits of $K_{d\,Fe-Mg}^{px-liq}$ as a function of pressure (Fig. 4b and c) are significant at the 1% significance level. As expected, considering the close relationship between pressure and temperature, expressions with temperature as the independent variable have similar regression statistics.

The pyroxenes in the CMASF experiments are quaternary solid solutions. In addition to the quadrilateral components, enstatite (En), ferrosilite (Fs) and wollastonite (Wo), they contain Tschermak's (Ts) component. In the CMASF system, as well as the CMAS system, all the Al in both orthopyroxene and clinopyroxene is expected to enter into the structure of these minerals as the Ts component, whereas in the CMASN system, the pyroxenes, clinopyroxene in particular, incorporate increasing amounts of jadeite (Jd) component with increasing pressure (Walter & Presnall, 1994). Although the Jd component must account for some of the Al in the pyroxenes in the CMASN system, no systematic differences in the Al content of the pyroxenes between the three systems are evident (Fig. 5), except that the CMASF orthopyroxene may have slightly less Al in the spinel lherzolite field than orthopyroxene from the two other systems. In both orthopyroxene and clinopyroxene the amount of Al increases rapidly with increasing pressure in the plagioclase lherzolite field, but remains almost unchanged in the spinel lherzolite field or increases slightly. The Al content is almost the same in orthopyroxene and clinopyroxene, and is apparently unaffected by the *mg*-number of the pyroxenes.

The Ca content of orthopyroxene in the CMAS, CMASN, and CMASF systems is similar, and does not

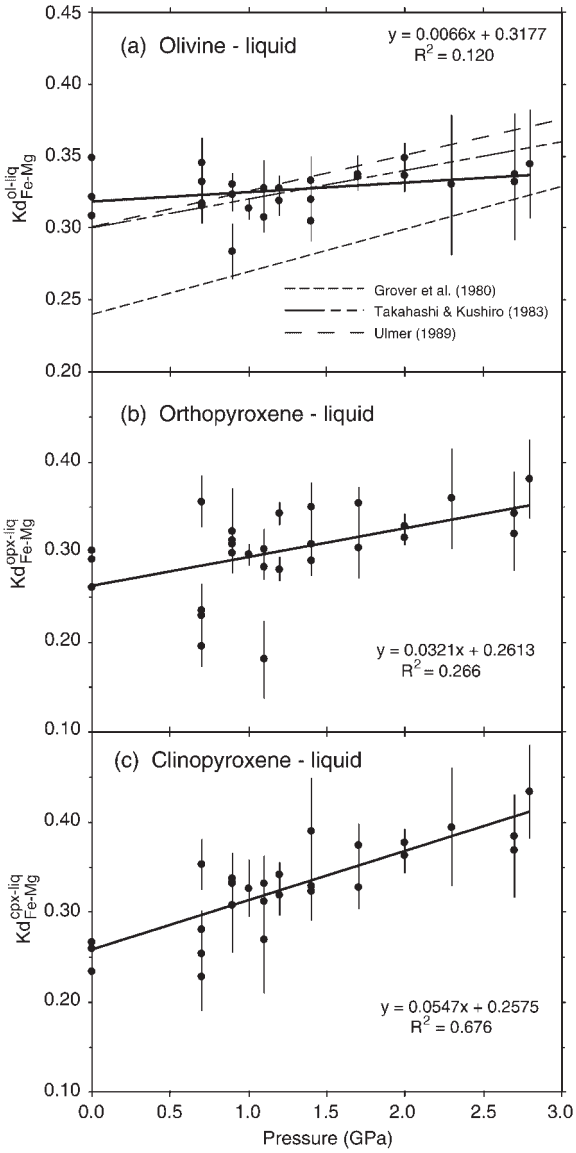

Fig. 4. $K_{d\,Fe-Mg}^{xl-liq}$ vs pressure. ●, CMASF data points, and the 0·1 MPa data are from Shi & Libourel (1991). Error bars denote propagated errors derived from 1σ of the electron microprobe analyses of coexisting olivine and glass. The bold lines are regression fits with pressure as the independent variable and $K_{d\,Fe-Mg}^{xl-liq}$ as the dependent variable (regression statistics shown). (a) $K_{d\,Fe-Mg}^{ol-liq}$ vs pressure. Displayed for comparison are lines from Grover *et al.* (1980), Takahashi & Kushiro (1983) and Ulmer (1989). The line of Grover *et al.* (1980) is both temperature and pressure dependent and has been arbitrarily calculated at temperatures where the CMASF isobaric univariant lines contain 8 wt % FeO. (b) $K_{d\,Fe-Mg}^{opx-liq}$ vs pressure. (c) $K_{d\,Fe-Mg}^{opx-liq}$ vs pressure.

change much with pressure and temperature. In contrast, the Ca content of clinopyroxene varies considerably both with pressure and temperature, and also between experimental systems (Fig. 6). To explain this, it is helpful to look at pyroxene relationships in a simpler system. Lindsley (1983) determined pyroxene phase relations in

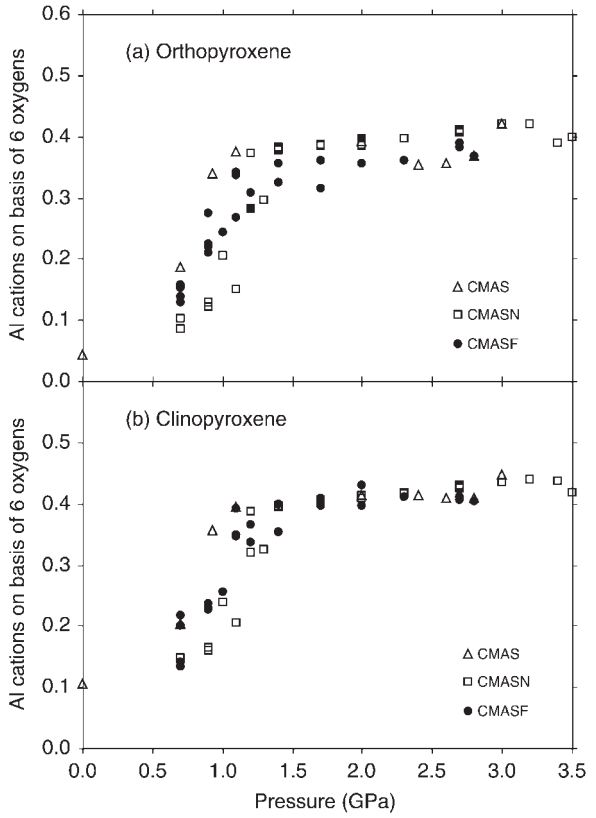

Fig. 5. The number of Al cations in (a) orthopyroxene and (b) clinopyroxene on the basis of six oxygen atoms as a function of pressure in the CMAS (Walter & Presnall, 1994; Gudfinnsson & Presnall, 1996; Milholland & Presnall, 1998), CMASN (Walter & Presnall, 1994) and CMASF systems. All experiments have the lherzolite phase assemblage in equilibrium with melt.

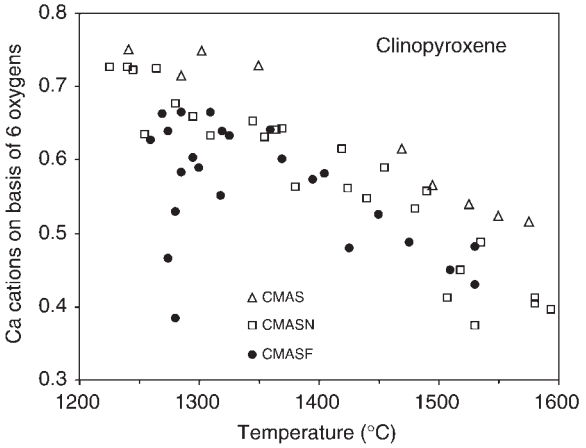

Fig. 6. Same as Fig. 5 for Ca in clinopyroxene.

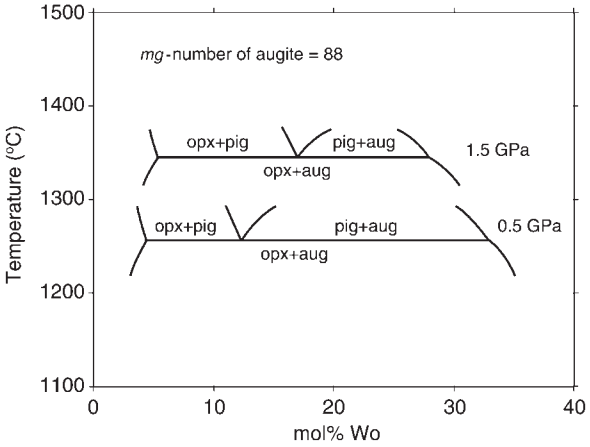

Fig. 7. Temperature vs mol % Wo in coexisting pyroxenes at 0·5 and 1·5 GPa pressure. The diagram has been drawn for phase relations with augite of *mg*-number 88. The other pyroxenes have slightly different *mg*-numbers.

the system En–Fs–Wo at pressures from 0·1 MPa to 1·5 GPa, and in Fig. 7 the phase relations at 0·5 and 1·5 GPa are sketched for a fixed *mg*-number in augite. The figure shows three two-pyroxene immiscibility gaps, and that isobarically, at a fixed *mg*-number in augite, there is an invariant phase assemblage involving three coexisting pyroxenes—orthopyroxene, pigeonite, and augite. At higher *mg*-numbers, the three-pyroxene invariant occurs at higher temperatures, and the augite becomes less calcic. The size of the pigeonite–augite solvus decreases with pressure and at pressures between 1·5 and 2·0 GPa, dependent on the *mg*-number of the system, it disappears entirely [see Bertka & Holloway (1993), and references therein, and Longhi & Bertka (1996)]. Therefore, in the pressure range 0·1 MPa to >1·5 GPa, these equilibria can be represented by a divariant surface along which the assemblage orthopyroxene + augite, on the low-temperature side, transforms to either orthopyroxene + pigeonite or augite + pigeonite, depending on the bulk composition of the system.

If the pyroxenes in the CMASF system were Al free, these phase relations could be used directly to determine if and where in P–T–X space the pyroxene transformation occurs in the CMASF system. However, the CMASF pyroxenes also contain a significant amount of Ts component, which increases the variance of the pyroxene transformation and changes the P–T–X relations. As no systematic study has been carried out to determine pyroxene stability in the En–Fs–Wo–Ts system with pressure, we can only make inferences about the position of the pyroxene transformation from our experimental data. The continuously gradual change in the Ca content of the CMASN clinopyroxenes (Fig. 6) indicates that the transformation was not encountered in these experiments. In the CMASF system, however, the transformation appears to be crossed and a transformation must occur

on the CMAS solidus from pigeonite to orthopyroxene. In the 0·1 MPa runs of Shi & Libourel (1991), the coexisting CMASF pyroxenes are augite and pigeonite with *mg*-numbers as low as 70. At the same pressure in the CMAS system Presnall *et al.* (1979) also found pigeonite and diopside coexisting, whereas at 0·7 GPa the stable low-Ca pyroxene was enstatite. Thus, at a pressure between 0·1 MPa and 0·7 GPa, there is an invariant point on the lherzolite solidus in the CMAS system generated by the change in pyroxene assemblage from pigeonite + diopside to enstatite + diopside. This invariant point becomes a univariant line in P–T space in the CMASF system and probably extends to higher pressures with increasing Fe content of the coexisting pyroxenes (Longhi & Bertka, 1996). At the 0·7 GPa isobaric univariant line containing the lherzolite assemblage in equilibrium with melt, we obtain orthopyroxene and augite coexisting with melts with up to 9 wt % FeO and never encounter low-Ca clinopyroxene. At 0·9 GPa, however, three of the most Fe-rich CMASF runs have clinopyroxene with highly variable Ca content, which may in fact represent two clinopyroxene phases. Consequently, these pyroxene compositions were not included in the phase parameterization. The transformation is not obvious in the higher-pressure data, and with higher Fe content the Ca content of the clinopyroxene seems to decrease only gradually, but the CMASF clinopyroxenes are systematically lower in Ca than the CMAS and CMASN clinopyroxenes in the plagioclase lherzolite stability field (Fig. 6). However, at 1·5 GPa Bertka & Holloway (1993) found pigeonite [or low-Ca clinopyroxene (Longhi & Bertka, 1996)] stable at the solidus of FeO-rich peridotite (*mg*-number = 75) coexisting with orthopyroxene.

Spinel

The spinel phase in the CMASF experiments is mostly a solid solution of the spinel component ($MgAl_2O_4$) and the hercynite component ($Fe^{2+}Al_2O_4$). The spinels also contain some CaO and SiO_2, but in many cases probably less than the analyses indicate because, as previously mentioned, the spinel grains were generally of small size. Therefore, in some cases the analytical volume may have exceeded the size of the crystals. Spinel is the crystalline phase likely to contain the most ferric iron, but because of the highly reducing conditions of the experiments, the amount of ferric iron is likely to be small. The good stoichiometry achieved for the spinels by assuming that all the Fe was ferrous also supports this contention. The Fe–Mg ratio of spinel is the highest of the crystalline phases and the results of multiple linear regression to our data indicate that the Fe–Mg exchange coefficient is virtually independent of pressure and temperature at an average $K_{d\,Fe-Mg}^{sp-liq}$ of 0·46 ± 0·02.

Anorthite

A few analyses of anorthite yielded nearly stoichiometric anorthite ($CaAl_2Si_2O_8$) with 0·3–0·5 wt % MgO and 0·4 wt % or less FeO.

MELTING OF MODEL LHERZOLITE IN THE CMASF SYSTEM

In a preceding section, the variation in the composition of all the lherzolite phases and coexisting melt in the CMASF system was described as a function of pressure and temperature. The phase equilibria thus described allow the melting of any arbitrary starting composition in the CMASF system to be modeled using the algebraic methods of Presnall (1986), provided that the starting composition can be expressed as a combination of all the lherzolite phases and melt at the P–T conditions of interest. In the following section we develop several CMASF mantle analog compositions. Then we use one of them to investigate various isobaric and polybaric melting processes in the upper mantle and to evaluate the applicability of the CMASF phase relations to modeling of melt generation in the upper mantle. The data of Dick & Fisher (1984) establish that MORBs appear to be produced by melting that does not extend beyond the disappearance of diopside or spinel. Therefore, the present work, which extends only this far, is relevant to the highly important case of MORB generation and probably also to other cases.

Mantle compositions in the CMASF system

CMASF components constitute ~98–99 wt % of the chemical composition of the mantle (Ringwood, 1975; Hart & Zindler, 1986; McDonough & Sun, 1995; see Table 4). The most important remaining oxides, Na_2O and Cr_2O_3, are most abundant in clinopyroxene and spinel, respectively (Basaltic Volcanism Study Project, 1981). Clinopyroxene is the phase that tends to be eliminated first from abyssal peridotites during the generation of MORBs (Dick *et al.*, 1984), whereas Cr-bearing spinel becomes highly refractory. Small amounts of spinel with high *cr*-number [= Cr/(Al + Cr)] may survive after high degrees of melting (Jaques & Green, 1980). Therefore, to lessen the effect of the absence of these components, when reconstructing a mantle composition in the CMASF system, we attempt to reproduce the mineralogy of the mantle, rather than simply renormalize the CaO, MgO, Al_2O_3, SiO_2 and FeO contents of natural peridotites. We use several estimates because the mineralogy is uncertain and depends on pressure and temperature in addition to bulk composition. The resulting bulk compositions are listed in Table 4. Also listed, for

*Table 4: Simplified mantle peridotite**

<c>	C88	C91	JDS	HZ	DF80	AMP	PUM	PMS
CaO	3·33	2·14	3·72	3·88	3·94	3·1	3·27	3·55
MgO	39·18	43·57	38·95	38·57	38·48	38·1	37·8	37·8
Al_2O_3	5·37	3·61	4·73	5·37	5·46	4·6	4·06	4·45
SiO_2	43·07	42·73	44·86	44·50	44·15	45·1	46·0	45·0
FeO	9·05	7·94	7·74	7·69	7·98	7·9	7·54	8·05
						98·8	98·67	98·85
mg-no.	88·5	90·7	90·0	89·9	89·6	89·6	90·0	89·3
Ca/Al†	0·84	0·80	1·06	0·98	0·97	0·91	1·09	1·08

*Compositions in weight percent.
†By weight.
C88 and C91 are compositions based on the mantle xenolith mode of Carter (1970), JDS is based on the mantle mode of Johnson *et al.* (1990), HZ is based on the mode of Kinzler & Grove (1992*b*), and DF80 is based the mode of residual abyssal peridotites (Dick & Fisher, 1984) added to a 1·2 GPa CMASF melt. Details are explained in text. AMP is average mantle pyrolite of Ringwood (1975). PUM is primitive upper mantle of Hart & Zindler (1986). PMS is pyrolite model of McDonough & Sun (1995). *mg*-number = 100Mg/(Mg + Fe) in mol fractions.

comparison, are the average mantle pyrolite of Ringwood (1975), the primitive upper-mantle composition of Hart & Zindler (1986), and the pyrolite model of McDonough & Sun (1995).

Compositions C88 and C91 are derived from the mode of fertile and partly depleted mantle xenoliths, respectively, at Kilbourne Hole, New Mexico (Carter, 1970). It is assumed that the xenoliths equilibrated at 30–40 km depth, that is, at ~1·2 GPa pressure. To derive the bulk compositions, we use the mineral modes of Carter (1970) but use mineral compositions from the CMASF system at the same pressure. The mineral compositions chosen are those coexisting with olivine of the same Fo content as observed by Carter (1970) in the Kilbourne Hole xenoliths. For the reconstruction of composition JDS, we use the mantle mode used by Johnson *et al.* (1990) in their geochemical modeling, and recalculate the bulk composition in an identical way to C88 and C91 assuming olivine of Fo_{90} composition. The composition HZ was similarly constructed using the mode of composition H&Zdep1 of Kinzler & Grove (1992*b*). DF80 is a combination of the average mode of residual abyssal peridotites of Dick & Fisher (1984), recalculated to 1·2 GPa CMASF composition and using minerals in equilibrium with olivine of $Fo_{90·7}$ composition, added to the coexisting melt in the proportion 80 wt % abyssal peridotite, 20 wt % melt.

The mineral mode in the CMASF system for the compositions above is strongly dependent on the pressure. For example, in the CMASF system the mantle analog composition JDS is composed of olivine, orthopyroxene, clinopyroxene, and spinel in the weight proportion 55: 25:18:2 at the solidus at 1·2 GPa, whereas at the solidus at 2·5 GPa the proportion is 56:17:26:1. The main difference is the large increase in the amount of clinopyroxene with increasing pressure and temperature, mostly at the expense of orthopyroxene. This can be anticipated from the fact that clinopyroxene is the main sink for Ca in the spinel lherzolite stability field; and, as previously demonstrated, the amount of Ca in clinopyroxene in the spinel field decreases drastically with increasing pressure. This is caused mostly by narrowing of the two-pyroxene immiscibility gap as temperature rises with pressure along the solidus curve and also the geotherm. Hence, more clinopyroxene is needed to accommodate Ca in the upper mantle as pressure increases.

Comparison of the melting behaviour of mantle analogs

For comparison of the melting behaviour of the five analog mantle compositions, isobaric batch melting has been modeled for all the compositions at 2·0 GPa in the spinel lherzolite stability field (Fig. 8). At 2·0 GPa the solidus temperatures of these compositions vary from 1424 to 1431°C, and the amount of melting varies from about 10 to 20% before either spinel or clinopyroxene is exhausted. Also, the temperature interval of 1·5–3°C over which the melting occurs is very small. There are three main observations. First, all trends are nearly linear. Second, in all cases the abundances of CaO, Al_2O_3 and SiO_2 in the melt increase very slightly with increasing degree of melting, whereas the increasing amounts of MgO and especially the decreasing amounts of FeO

change more strongly. Third, the abundances of CaO, Al_2O_3 and SiO_2 in the melt are affected very little by the bulk composition, whereas the amount of MgO is slightly more sensitive to the bulk composition. It is the FeO content in the melt, however, that varies by far the most in response to changing source composition. Modeling of the melting of different source compositions in the plagioclase lherzolite stability field is not shown, but the general trends are essentially the same as in the spinel lherzolite stability field.

The differences in the concentrations of the oxides in the melts do not simply reflect their concentrations in the source; comparing melting among different bulk compositions, variations in the CaO, Al_2O_3, and SiO_2 contents are far less in the melts than in the respective bulk compositions. However, when the mantle analogs are melted to similar degree, their original *mg*-numbers correlate positively with the CaO, MgO, Al_2O_3, and SiO_2 concentrations of the coexisting melts, and negatively with the FeO contents. This is a further indication that along isobaric univariant lines in the CMASF system there is not much change in the melt composition, except in the MgO and FeO abundances, and that the temperature at which a lherzolite composition will start to melt along such lines is to a large extent decided by the *mg*-number of the lherzolite. This can also be anticipated from the fact that Fe–Mg exchange is the main solid solution in the system.

Figure 9 shows an excellent linear correlation between the *mg*-numbers of the model lherzolites and those of melts at the 2·0 GPa solidus, 10% melts at the same pressure, and solidus melts at 0·9 GPa. This correlation is not an artifact of the procedure for constructing the lherzolite compositions. Melting models for the mantle compositions of Ringwood (1975), Hart & Zindler (1986), and McDonough & Sun (1995) normalized to CMASF components yield solidus compositions that fall close to the lines. Figure 9 shows that the lines shift with pressure and increasing degree of melting but the linear correlation holds and the lines have nearly identical slopes. If the *mg*-numbers of the melts are plotted against those of the coexisting residues, the points lie on a single line at each pressure and are shifted to higher values with increasing degree of melting.

From these observations it appears that the most critical aspects of the composition of a model lherzolite in the CMASF system are the FeO and MgO contents. Differences in the amounts of the other oxides mainly affect the proportions of the crystalline phases, and hence which phase is first exhausted and how much melting occurs before that eventuality, but the amounts of these oxides have only a small effect on the composition of the melt. This effect is illustrated in a very simple way in the system MgO–FeO–SiO_2 (Bowen & Schairer, 1935). For a three-phase triangle with the equilibrium assemblage olivine + enstatite + liquid, the proportions of enstatite and olivine for a bulk composition (mantle source) along the base of the three-phase triangle can vary from nearly zero to nearly 100%, yet the composition of the liquid in equilibrium with these phases remains the same. Composition DF80 has FeO content and *mg*-number close to the mantle compositions suggested by Ringwood (1975), Hart & Zindler (1986), and McDonough & Sun (1995) (Table 4). It is therefore proposed as a good analog for average upper-mantle lherzolite, and will be used in the following analysis of the melting behaviour of model lherzolite in the CMASF system.

Isobaric melting trends

Figures 10 and 11 illustrate isobaric batch melting trends of DF80 as a function of melting extent in the plagioclase lherzolite stability field at 0·8 GPa and in the spinel lherzolite stability field at 2·0 GPa, respectively. Also included are comparable trends from the CMASN system for melting of model lherzolite A (Walter & Presnall, 1994), and the melting trends of H&Zdep1 from Kinzler & Grove (1993). The algorithm of Kinzler & Grove (1993) is thermodynamically guided and is based on melting experiments, mainly on natural rocks. This comparison serves to illustrate the general trends and to evaluate the suitability of the CMASF data for modeling of mantle melting. The equilibrium batch melting behaviour of the CMASF and CMASN mantle analogs is similiar in the plagioclase lherzolite stability field in the sense that the melt compositions change very little as melting progresses (Fig. 10). Changes in the liquid composition when H&Zdep1 is melted are also relatively modest. The greatest difference between the melting trends in the CMASF model and in the other two models is the lower SiO_2 in the former. The difference decreases, however, as the amount of melting increases. This can be explained by the tendency of alkalis to reduce the activity coefficient of SiO_2 in silicate melts; so that at a constant SiO_2 activity, increasing amounts of alkalis lead to increasing SiO_2 content of the melts (Hirschmann *et al.*, 1998). The CMASF melt also has higher CaO content than the other two, probably because of Ca–Na exchange, that is, in the Na_2O-free CMASF system Ca tends to substitute for Na. Correspondingly, in the plagioclase lherzolite stability field the plagioclase being melted in the CMASF system is end-member anorthite, but in the other two systems the plagioclase is Na_2O-bearing with lower amounts of CaO.

In the spinel field (Fig. 11), both model lherzolite A and H&Zdep1 have curved melting trends, whereas the DF80 melting trends are nearly linear, but, importantly, as the degree of melting increases, the three trends tend to converge. The MgO trend for model lherzolite A is

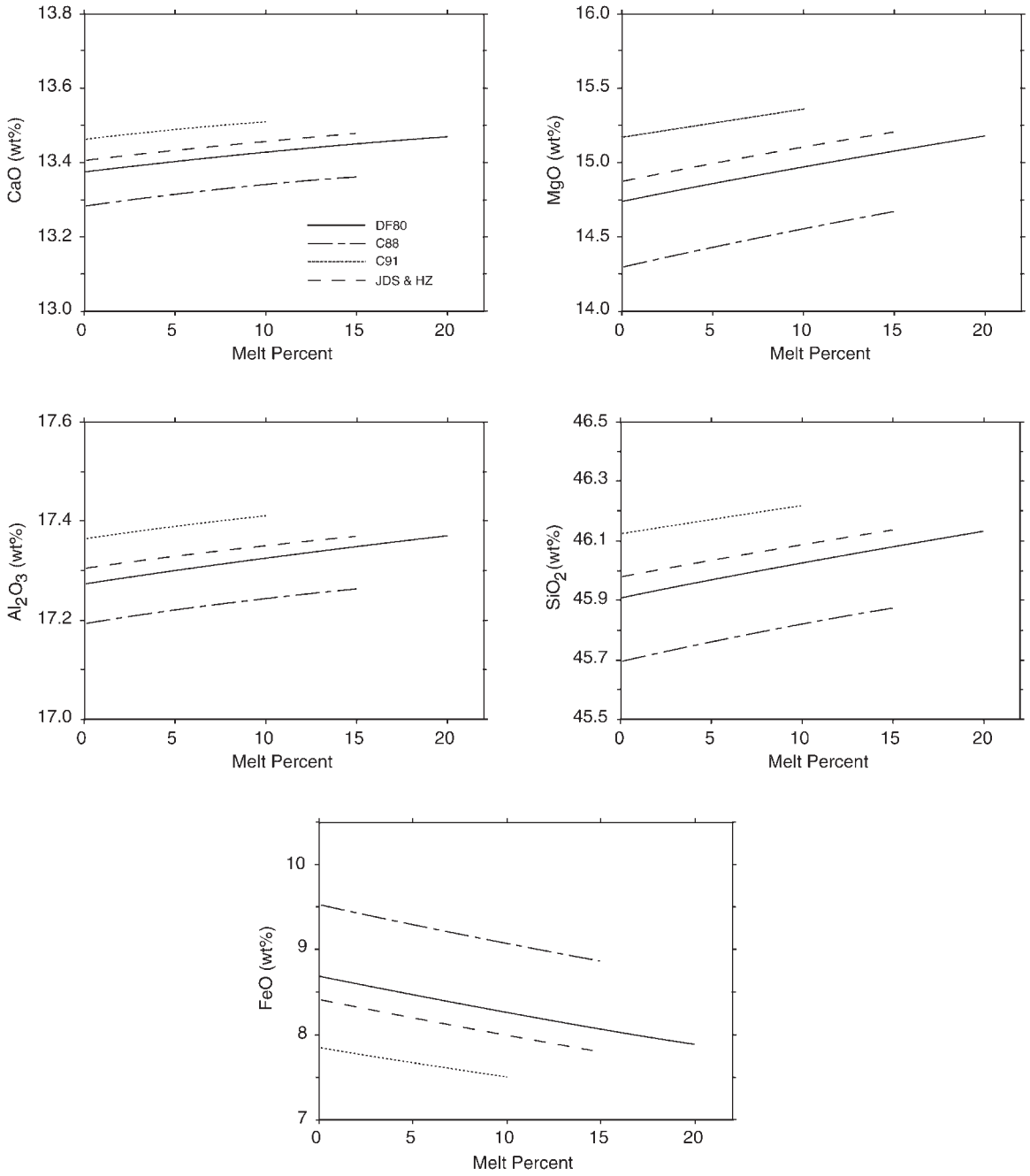

Fig. 8. Variation of CaO, MgO, Al_2O_3, SiO_2 and FeO in isobaric melts with degree of melting (wt %) at 2·0 GPa. The lines indicate compositional variations for the various mantle analogs (see Table 4). The nearly identical trends for compositions JDS and HZ are shown as one line.

an exception. It has the expected curved shape, but goes to higher concentrations than if it were consistent with the other trends. It must be kept in mind, however, that the CMASN system is FeO free. Judging from the melting trends in the CMASF system discussed above, adding FeO to the CMASN system would not just dilute all the other oxides, but would lower the MgO content of the melt more than simple dilution would cause. When the algorithm of Kinzler & Grove (1993) is used to model melting of composition H&Zdep1 at 2·0 GPa, the FeO abundance in the melt increases initially but starts to level off or even decrease at higher extent of melting. In

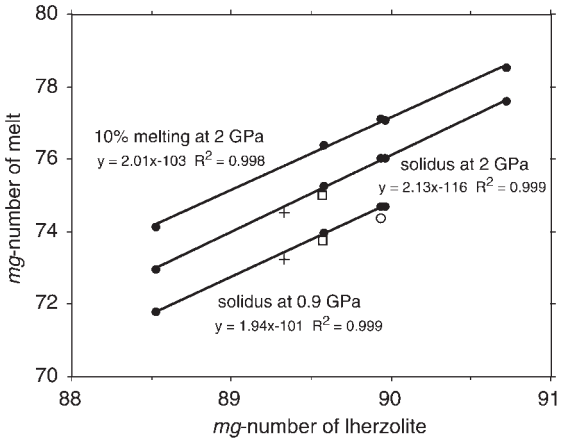

Fig. 9. Diagram illustrating the relationship between the *mg*-numbers of lherzolite compositions (listed in Table 4) and the *mg*-numbers of their solidus melts at 2·0 GPa and 0·9 GPa, and their 10% melts at 2·0 GPa. The lines are regression fits. □, average mantle pyrolite of Ringwood (1975); ○, primitive upper mantle of Hart & Zindler (1986); +, pyrolite model of McDonough & Sun (1995). These three compositions are not included in the regression. All three compositions lose a phase before 10% melting is reached, and the primitive upper-mantle composition of Hart & Zindler (1986) does not melt at 2·0 GPa in equilibrium with all the lherzolite phases.

contrast, the FeO abundance in the CMASF system steadily decreases as melting progresses. Langmuir *et al.* (1992) commented that during isobaric melting of mantle compositions the abundances of FeO and MgO in the liquid are initially low because of the high concentration of alkalis, which have the effect of raising the distribution coefficients of Fe and Mg between olivine and liquid.

The main reason for the difference in the melting behaviour between the plagioclase and the spinel field, and between the Na_2O-bearing and the Na_2O-free systems, is probably the strong effect of Na_2O on the stability and the composition of the melt in the spinel lherzolite field at small to modest degrees of melting. In the spinel field, Na is considerably more incompatible than in the plagioclase field (Walter & Presnall, 1994), so Na_2O is highly concentrated in the early melt. As the amount of melt increases, Na_2O becomes more diluted in the melt, its effect on the melt composition diminishes, and the liquidus phase relations in the Na_2O-bearing and the Na_2O-free systems become more alike. Mysen & Kushiro (1977) also observed sharp dips in the melting curves of natural peridotites close to their solidi and suggested this is caused by the depolymerizing effect of alkalis in the melt. From this we expect near-fractional melting behaviour of mantle compositions in the CMASF system to resemble the melting behaviour of natural lherzolite even more than batch melting after the initial few percent melting, because a large proportion of Na_2O and other incompatible elements would be removed with the initial melt, leaving the remaining mantle depleted in Na_2O. In the spinel field, model lherzolite A starts to melt at a lower temperature than composition DF80, but high degrees of melting are reached in the CMASN system only at a much higher temperature than in the CMASF system (Fig. 12). At high degrees of melting the temperature of model lherzolite A approaches the solidus temperature of the lherzolite phase assemblage in the CMAS system. Furthermore, the data from the CMASF and CMASN systems suggest that Na_2O is the critical melt component for reducing the activity of SiO_2 in the melt (Hirschmann *et al.*, 1998), causing modest enrichment of SiO_2 in the melt at low degree of melting, especially in the spinel lherzolite field. However, the simple system data do not confirm the large increases in SiO_2 seen in the melting experiments of Baker *et al.* (1995) (Hirschmann *et al.*, 1998). From all this evidence, we deduce that melting relations of model lherzolite in the system CMAS + Na_2O + FeO would closely mimic the melting behaviour of upper-mantle lherzolite.

Figure 13, a molecular normative diagram, depicts the isobaric batch melting trends for DF80 in the spinel and plagioclase lherzolite fields. At 0·5 GPa in the plagioclase lherzolite stability field, clinopyroxene is exhausted after only incipient melting, but melting before clinopyroxene exhaustion increases with pressure and reaches ~20% melting at the plagioclase to spinel lherzolite transition. In the spinel lherzolite stability field, spinel is the first phase to be eliminated, just before clinopyroxene. This occurs after ~22% melting in the whole stability range of spinel lherzolite. During isobaric melting, it can be seen that the compositional range of the melts is always very small, as discussed above.

Complications arise in the melting behaviour around the transitions from garnet to spinel lherzolite and spinel to plagioclase lherzolite. Figure 14 is a P–T diagram of the region around the transition from spinel lherzolite to plagioclase lherzolite and shows melting contours for equilibrium melting of composition DF80. The position of the P–T univariant line along which the transition occurs is independent of the bulk composition, unlike the position of the solidus and the melting contours. We explain the changes across the transition in the melting behaviour of a mantle composition in the CMASF system by describing the melting of DF80 at four isobars. At 1·2 GPa the subsolidus assemblage for DF80 is spinel lherzolite, which starts to melt at ~1320°C, and at 1325°C spinel is eliminated. At a slightly lower pressure, for example at 1·175 GPa, the phase assemblage immediately below the solidus is plagioclase–spinel lherzolite that starts to melt at the transition line at ~1318°C according to the isobarically invariant melting reaction ol + an = opx + cpx + sp + liq. Melting continues at this temperature until anorthite is exhausted after a few percent melting, but then continues with rising temperature. After ~22% melting no spinel remains. At

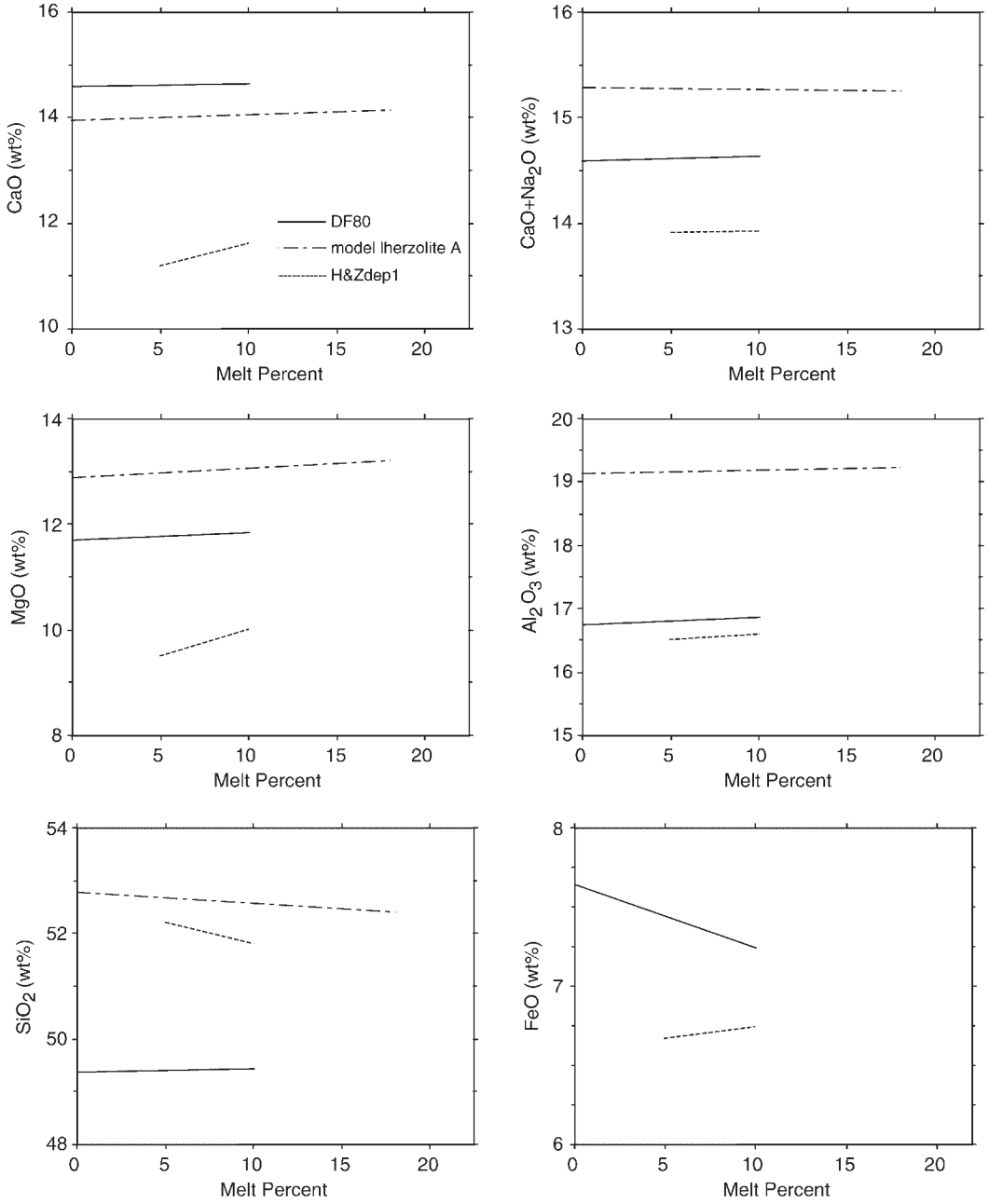

Fig. 10. Variation of CaO, CaO + Na_2O, MgO, Al_2O_3, SiO_2 and FeO in isobaric melts with degree of melting (wt %) in the plagioclase lherzolite field at 0·8 GPa. The various lines indicate compositional variations in the melting models: the continuous lines denote the melting trend of composition DF80 in the CMASF system; the dash–dot line that of model lherzolite A in the CMASN system (Walter & Presnall, 1994); and the dotted line the melting trend of H&Zdep1 (Kinzler & Grove, 1993).

lower pressure still, for example, at 1·15 GPa, the phase assemblage just below the solidus is plagioclase lherzolite. At this pressure melting starts at ~1312°C and melting of plagioclase lherzolite progresses with rising temperature. After 10–15% melting, the transition is reached at 1315°C, spinel appears, and melting progresses at a fixed temperature according to the transition reaction above, but with slightly different phase proportions in the melting reaction. When anorthite is exhausted after ~20% melting, temperature continues to rise but melting of spinel lherzolite ends after 2% more melting when no more spinel remains. At all pressures lower than ~1·14 GPa the phase assemblage just below the solidus is plagioclase lherzolite. Melting progresses with continuously rising

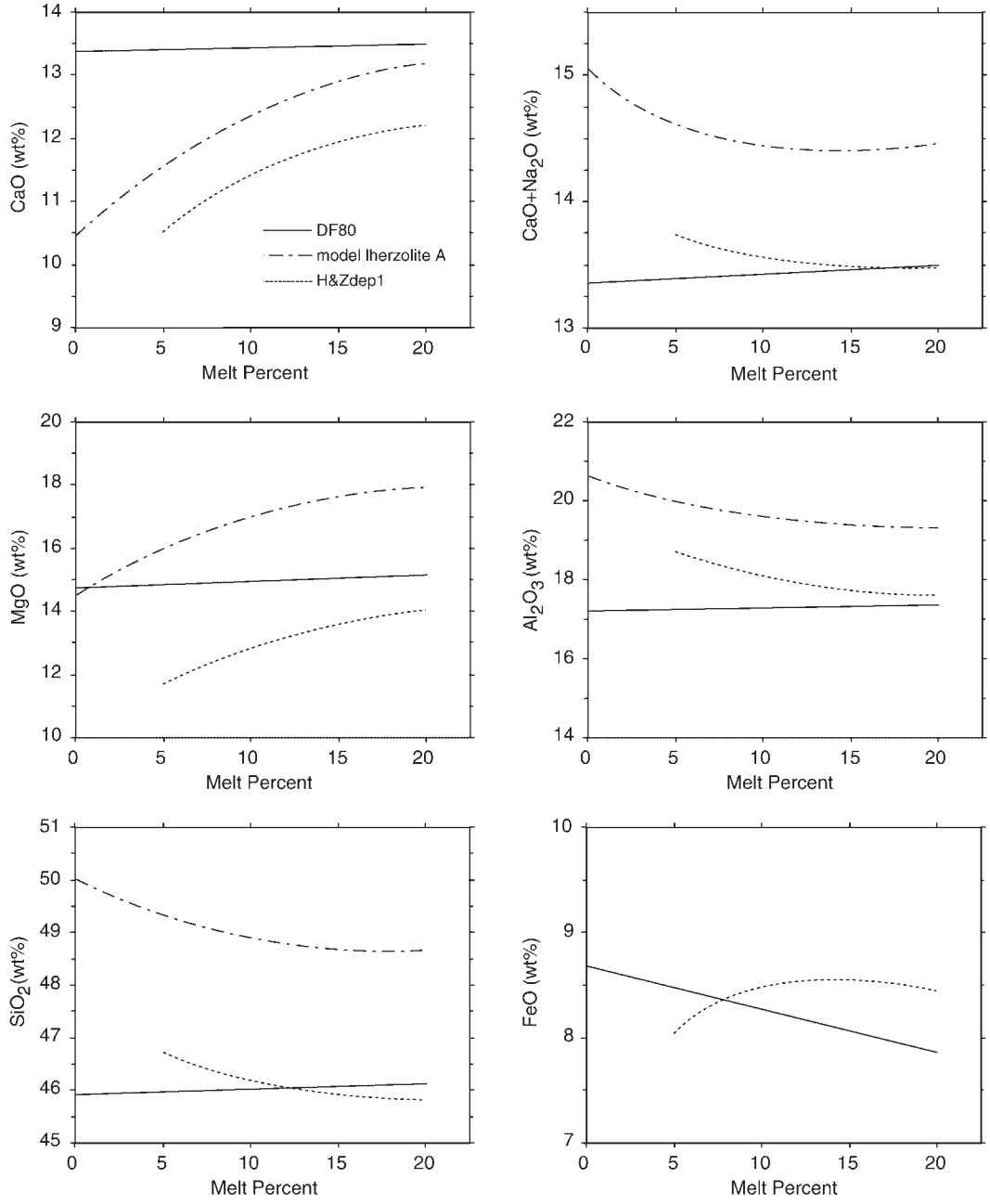

Fig. 11. Same as Fig. 15 in the spinel lherzolite field at 2·0 GPa.

temperature until clinopyroxene is entirely consumed and melting continues in the presence of olivine, orthopyroxene and anorthite only. Comparison with melting at the spinel to plagioclase lherzolite transition in the CMASN system (Walter & Presnall, 1994, fig. 9) shows that comparable changes occur in the melting behaviour of the CMASN mantle analog model lherzolite A as in the melting behaviour of DF80. The main difference in the melting behaviour of the two mantle analogs is that the melting interval of lherzolite A is much larger than that of DF80.

Polybaric melting trends

We are now able to evaluate how well melting compositions generated by decompression melting in the upper mantle can be predicted by using the CMASF

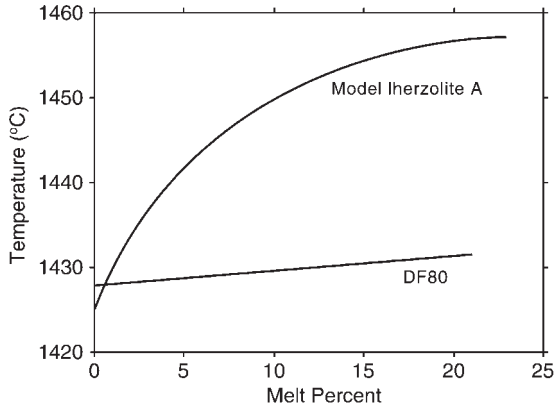

Fig. 12. Temperature vs degree of melting (wt %) at 2·0 GPa for composition DF80 in the CMASF system and composition model lherzolite A in the CMASN system (Walter & Presnall, 1994).

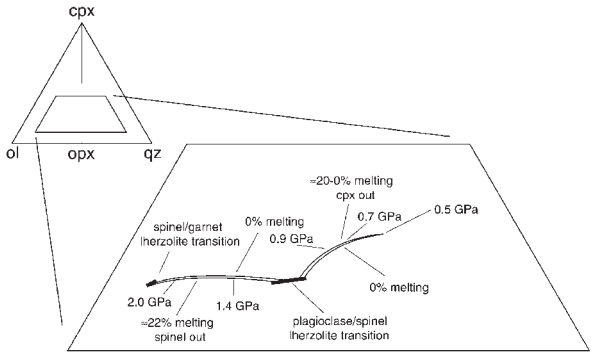

Fig. 13. Molecular normative diagram depicting isobaric melting trends for composition DF80 in the spinel and plagioclase lherzolite stability fields. The melting trend is presented by two fine lines, where one line (0% melting) is the locus of initial liquid compositions at the solidus as a function of pressure and the other is the locus of melt compositions where the first crystalline phase is exhausted. Because the composition DF80 does not melt with all the lherzolite phases present below 0·5 GPa pressure, the melting trend starts at this pressure. The bold lines indicate the transitions on the solidus in the CMASF system from garnet to spinel lherzolite and spinel to garnet lherzolite. Comparison with Fig. 2b, which shows the whole compositional trend from the solidus to 10% melting at 0·1 MPa–3·0 GPa, reveals the narrow melting range of composition DF80.

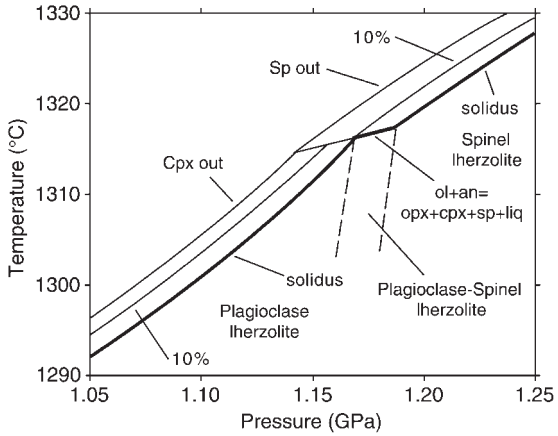

Fig. 14. Pressure–temperature diagram illustrating equilibrium melting of composition DF80 in the region around the spinel to plagioclase lherzolite transition. Bold lines indicate the solidus of this composition and the fine continuous lines (except the ol + opx + cpx + an + sp + liq univariant curve) are contours for 10% melting and melting where the first phase is exhausted (spinel in the spinel lherzolite stability field and clinopyroxene in the plagioclase lherzolite stability field). This is ∼22% melting in the spinel lherzolite stability field and an amount in the plagioclase lherzolite stability field that decreases with decreasing pressure from ∼22% at the transition. The three subsolidus phase assemblages, plagioclase lherzolite, spinel lherzolite, and plagioclase–spinel lherzolite, are labeled in the diagram. The transition region in the subsolidus, delimited by dashed lines, is divariant. Its slope is uncertain but here it is assumed that the slope is similar to that of a comparable transition in the CMAS system (Presnall *et al.*, 1979) where the transition is univariant.

dataset, and under what conditions the CMASF data would be most applicable. First, it was noted that different datasets tend to yield converging melting trends with increasing degree of melting, and that this is especially true for melting in the spinel lherzolite stability field. Second, incompatible elements, including Na, tend to be depleted at an early stage during fractional melting. Hence, the CMASF dataset is best suited to model generation of high-degree melts during fractional melting or melting of highly depleted lherzolite sources that have not lost any of their major lherzolite phases. Third, compared with more complex systems, the melting behaviour of mantle compositions in the CMASF system limits the compositional range that can be attained in polybaric melting models. A corollary of these conclusions is the prediction that if primary basalts are generated by fairly high degrees of fractional, or near-fractional, melting and later accumulation of the incremental melts, then the compositional range will be limited by a closer approach to invariant melting behaviour as melting progresses and as long as all the major lherzolite phases are still present. It should be kept in mind, however, that even the most depleted primitive basalt glasses from mid-ocean ridges still contain significant amount of Na_2O, so that Na is certain to have a considerable effect on the melting relations of primary MORB liquids.

In detail, compositions obtained from polybaric models for melt generation in an upwelling part of the mantle depend on many factors, for example, bulk composition, initial pressure of melting, melt generation per interval of mantle ascent, melt fraction required before extraction occurs, and the shape of the melting regime (e.g. Langmuir *et al.*, 1992). However, because of the limited compositional range of melts generated in the CMASF system, a simple model suffices to demonstrate the plausible range in melt compositions. For illustration of polybaric melting in the CMASF system, we consider a simple

near-fractional polybaric model for composition DF80. In this calculation, melting starts at different pressures, but in all cases ~1 wt % melt is generated per 0·1 GPa of mantle ascent. After each 0·1 GPa lowering of pressure, a 1% melt batch is removed and the bulk composition is recalculated. Hence, temperature is treated as an independent variable and is adjusted to yield the desired melt fraction. Melting continues until the elimination of the first crystalline phase; and at the end of the calculation, all the melts generated are accumulated. This model is similar to melting in the columnar-shaped melting regime (Langmuir *et al.*, 1992) that has been associated with decompression melting in response to active upwelling. In this simple model, we ignore a possible increase in melt productivity with decreasing pressure during adiabatic upwelling (Asimow *et al.*, 1997), as well as possible thermal effects and some melt consumption during the transition from spinel to plagioclase lherzolite (Asimow *et al.*, 1995). This last omission is justified by the observation that, in the CMASF system, melt produced in the pressure range of the transition reaction is only a small fraction of the total accumulated melt (see below).

One result from this model is that the higher the initial pressure of melting, the greater the final degree of melting before the first crystalline phase (clinopyroxene) is eliminated. If melting starts at 2·7 GPa, clinopyroxene is exhausted at 0·9 GPa after almost 18% melting. If melting starts at 2·0 GPa, DF80 yields ~12% melt, and if melting starts at 1·5 GPa only 9% melt is generated before exhaustion of clinopyroxene at 0·7 GPa. Another finding, in agreement with the proposal of Klein & Langmuir (1987), is that the FeO content of the accumulated melts increases with the average pressure of melting (Fig. 15). However, the range in FeO content yielded by our model is very small, ~0·5 wt %. This range would increase if melting is sometimes curtailed at higher pressures long before the exhaustion of one of the main lherzolite phases. Because of the lack of data from the garnet lherzolite stability field, we are unable to quantify the effect of a large amount of melting at pressures higher than that of the garnet to spinel lherzolite transition on the FeO content of the accumulated melts. The maximum range in FeO from melting DF80, obtained by considering instantaneous melts before accumulation, can be as much as 2 wt %. As pointed out by Langmuir *et al.* (1992), the presence of a large amount of alkalis lowers the amount of FeO in small degree melts, which might extend the range in FeO content of natural melts compared with the CMASF melts.

For the case in which polybaric melting starts at 2·7 GPa, Fig. 16 shows the instantaneous melt compositions at each pressure from 2·7 to 0·9 GPa. Also shown is the final accumulated melt composition. Because of the insensitivity of the melting process to lherzolite starting composition, all plausible source compositions will yield instantaneous melts close to the trend shown on Fig. 16, all accumulated melts will lie close to the relatively small area defined by the trend, and mixtures in any proportion of the batch compositions will yield a limited compositional range.

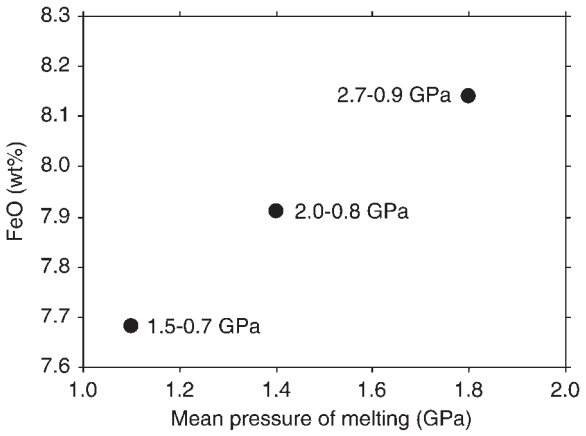

Fig. 15. FeO content of melts vs mean pressure of melting. ●, accumulated melt compositions generated by melting of composition DF80 in a near-fractional melting process (see text). The pressure range of melt generation is indicated on the diagram for each point.

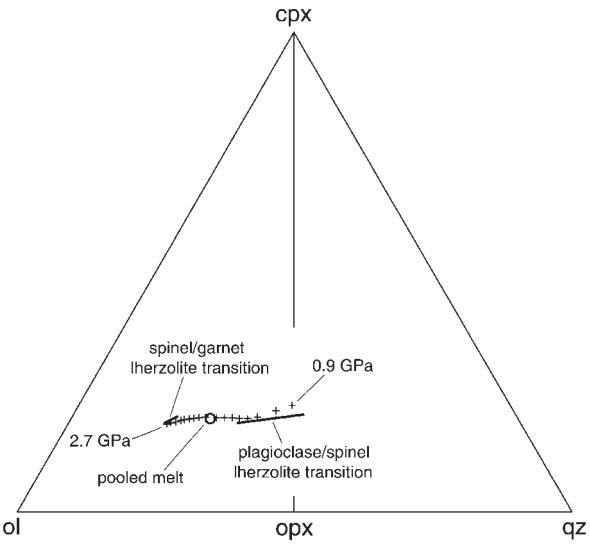

Fig. 16. Molecular normative diagram showing melt compositions when composition DF80 is melted in a near-fractional process at 2·7–0·9 GPa (see text). +, instantaneous melts at 0·1 GPa intervals; ○, final accumulated melt composition.

Melting reactions

Melting reactions indicate in what proportions the crystalline phases enter the melt. At isobaric invariant points, such as the phase equilibria involving the lherzolite phase

assemblage coexisting with melt in the CMAS system, all phases have fixed composition and uniquely defined melting reactions occur and continue as long as all the phases are present, independent of the bulk composition. However, for isobarically univariant phase relations that include solid solutions, such as the CMASF phase relations presented here, the melting reactions depend on the bulk composition. Furthermore, the composition of the melt changes continuously as melting progresses, and the fictive extracts (Morse, 1980; Walter *et al.*, 1995) from the crystals, which enter the melt, generally have different compositions from the crystals themselves, which accordingly change continuously in composition. The melting reactions at isobaric invariant points can be obtained by the determinant method of Korzhinskii (1959) but in the case of univariant phase relations this method cannot be applied. Instead, the tangent rule (Morse, 1980) is a commonly applied method but is inaccurate when, in addition to the melt composition, the compositions of the crystalline phases change. In this case, the mass-proportion method of Walter *et al.* (1995) can be used, and this is the method we use to calculate melting reactions in the CMASF system for composition DF80 (Table 5).

In the CMASF system, the form of the melting reaction shows important changes with pressure. At the highest pressure in the spinel lherzolite field, both olivine and orthopyroxene crystallize when the temperature is raised during isobaric batch melting, or in other words, they are in reaction relationship with the melt. The proportion of orthopyroxene is significantly greater than the proportion of olivine in the reaction, and judging from data in both synthetic and natural systems, orthopyroxene is the lone phase in reaction relationship with the melt in the garnet lherzolite field close to the spinel to garnet lherzolite transition (e.g. Davis, 1964; O'Hara & Yoder, 1967; Mysen & Kushiro, 1977; Herzberg *et al.*, 1990; Bertka & Holloway, 1993; Walter *et al.*, 1995; Gudfinnsson & Presnall, 1996; Milholland & Presnall, 1998; Walter, 1998). At lower pressures in the spinel lherzolite field, proportionally more olivine crystallizes when the temperature is raised, and just below 2·0 GPa orthopyroxene is no longer in reaction relationship with the melt during melting of composition DF80. Comparable changes occur in the melting reaction for lherzolite compositions in the CMAS (Gudfinnsson & Presnall, 1996) and CMASN (Walter *et al.*, 1995) systems, but the change in the relationship of orthopyroxene with liquid occurs at a higher pressure in the CMAS system and at a slightly lower pressure in the CMASN system during melting of composition model lherzolite A. However, the *mg*-number of the CMASF mantle composition has a strong influence on the pressure above which orthopyroxene changes to reaction relationship with the melt on the solidus. For example, this happens at ~2·1 GPa for composition C91 (*mg*-number = 90·7; see Table 4), whereas it happens at ~1·9 GPa for composition C88 (*mg*-number = 88·5). This is in good agreement with the observation of Bertka & Holloway (1993), who found that at 10–20°C above the solidus of an iron-rich mantle composition (*mg*-number = 75) at 1·5 GPa, both olivine and orthopyroxene are in reaction relationship with the melt. From its reaction coefficients, it can be seen that clinopyroxene is the phase that contributes the most to the melt in the spinel lherzolite field, whereas spinel contributes relatively little. None the less, spinel is the first phase exhausted in the spinel lherzolite field during equilibrium melting, but at that point only very small amounts of clinopyroxene remain. This may be close to what commonly happens during basalt generation in the mantle, as Carter (1970) found that clinopyroxene and spinel disappear almost at the same time as residual lherzolites from Kilbourne Hole become more depleted. In the plagioclase lherzolite field, olivine is in reaction relationship with the melt, in small amounts near the transition, but in increasing amounts as the pressure decreases. Clinopyroxene, orthopyroxene and plagioclase all contribute significant amounts to the melt in the plagioclase lherzolite field. A melting reaction at 1·2 GPa shows that the amount of melt participating in the reaction along the plagioclase to spinel lherzolite transition is small. Kinzler & Grove (1992*a*) observed similar changes in melting reactions in their experiments. Based on experiments containing iron-rich melts (*mg*-numbers 62 and 53), they found both olivine and orthopyroxene in reaction relationship with the melt at 1·6 GPa, and at lower pressures, both in the spinel and plagioclase lherzolite stability fields, olivine is the only phase in reaction relationship with the melt.

Comparisons between isobaric batch melting at the solidus and after 20% melting, between isobaric near-fractional melting and isobaric batch melting, and between isobaric batch melting and polybaric near-fractional melting, all show relatively small differences in the melting reactions (Table 5). This is consistent with the small changes in melt composition as melting progresses, as discussed above. Table 5 also compares melting reactions of DF80 and the CMASN composition model lherzolite A (Walter *et al.*, 1995). This comparison reveals strong similarities between the melting reactions in the two systems, especially when the reactions are assessed over long melting intervals. Walter *et al.* (1995) showed that when assessed over long melting intervals, there is very good agreement between melting reactions in the CMASN system and reactions inferred from experiments on natural compositions. In this case, the reactions also compare favorably with melting reactions of model lherzolite in the CMAS system (Gudfinnsson & Presnall, 1996). The largest difference in the reactions is at the solidus, but at that point the CMASN melts contain

Table 5: Melting reactions (weight proportions)*

Isobaric batch melting: instantaneous solidus melting reactions	
2·7 GPa	92 Cpx + 8 Sp = 69 Liq + 5 Ol + 26 Opx
2·0 GPa	91 Cpx + 9 Sp = 84 Liq + 13 Ol + 3 Opx
2·0 GPa (CMASN†)	91 Cpx + 9 Sp = 72 Liq + 9 Fo + 19 Opx
1·7 GPa	8 Opx + 82 Cpx + 10 Sp = 83 Liq + 17 Ol
1·0 GPa	20 Opx + 40 Cpx + 40 An = 99 Liq + 1 Ol
0·7 GPa	30 Opx + 35 Cpx + 35 An = 95 Liq + 5 Ol
0·7 GPa (CMASN)	24 Opx + 26 Cpx + 50 Pl = 95 Liq + 5 Fo
Isobaric melting at 2·0 GPa: instantaneous reactions after 20% melting	
Batch melting	3 Opx + 88 Cpx + 9 Sp = 86 Liq + 14 Ol
Near-fractional melting‡	3 Opx + 87 Cpx + 10 Sp = 87 Liq + 13 Ol
Polybaric near-fractional melting: 2·7–0·9 GPa§	
2·7 GPa	92 Cpx + 8 Sp = 69 Liq + 5 Ol + 26 Opx
2·0 GPa	91 Cpx + 9 Sp = 86 Liq + 13 Ol + 1 Opx
1·7 GPa	10 Opx + 80 Cpx + 10 Sp = 83 Liq + 17 Ol
1·0 GPa	24 Opx + 37 cpx + 39 An = 99 Liq + 1 Ol
Isobaric batch melting at 2·0 GPa: melting interval	
0–1%	91 Cpx + 9 Sp = 85 Liq + 13 Ol + 2 Opx
0–5%	91 Cpx + 9 Sp = 86 Liq + 13 Ol + 1 Opx
0–5% (CMASN)	5 Opx + 83 Cpx + 12 Sp = 88 Liq + 12 Fo
0–20%	1 Opx + 90 Cpx + 9 Sp = 86 Liq + 14 Ol
0–20% (CMASN)	5 Opx + 84 Cpx + 11 Sp = 86 Liq + 14 Fo
Isobarically invariant melting along plagioclase to spinel lherzolite transition	
1·2 GPa¶	47 Ol + 53 An = 2 Liq + 8 Opx + 71 Cpx + 19 Sp
1·3 GPa (CMASN)	30 Fo + 70 Pl = 72 Liq + 16 Opx + 4 Cpx + 8 Sp

*Melting of composition DF80, unless otherwise indicated, using parameterization in Table 3. Mass proportions of phases participating in the reactions. Determined with the mass-proportion method (Walter *et al.*, 1995). Liq, liquid; Ol, olivine; Fo, forsterite; Opx, orthopyroxene; Cpx, clinopyroxene; Sp, spinel; An, anorthite; Pl, plagioclase.
†Melting of composition model lherzolite A in the CMASN system (Walter *et al.*, 1995).
‡Melt increments of 1%.
§Details of melting model explained in text.
¶Reaction determined with the method of Korzhinskii (1959).

significant amounts of Na. The concentration of Na in the melt should rapidly diminish as melting progresses, especially during near-fractional melting, and the melting reactions in the CMAS, CMASN, and CMASF systems become similar. This shows that the melting reactions for simplified mantle compositions in the CMAS, CMASN, and CMASF systems all provide good approximations of melting reactions in the mantle during most of the melting process.

CONCLUSIONS

Addition of FeO to the CMAS system causes the solidus temperature of simplified lherzolite to fall by only 3–5°C for every 1 wt % increase in the FeO content of the coexisting liquid. The transition on the lherzolite liquidus in the CMASF system from spinel to plagioclase lherzolite has a positive Clapeyron slope with the spinel lherzolite phase assemblage on the high-temperature side. The P–T slope of the transition is almost identical to the slope of the comparable transition in the CMASN system (Walter & Presnall, 1994). FeO and MgO exhibit the greatest variation of all the oxides in the melt with degree of melting of lherzolite in the CMASF system; the amount of FeO decreases and the amount of MgO increases as melting progresses. The coefficients for the exchange of Fe and Mg between the crystalline phases and liquid, $K_{\mathrm{d\,Fe\text{–}Mg}}^{\mathrm{xl\text{–}liq}}$, show simple and predictable behaviour with pressure and temperature. The coefficients for olivine and spinel appear to be almost independent of pressure and temperature in the range of the experiments, whereas the coefficients for the pyroxenes increase with pressure

and temperature. By comparing melting trends in the CMASF system with melting trends in the CMASN system (Walter & Presnall, 1994) and with the model of Kinzler & Grove (1993), it is shown that Na_2O has a strong effect on phase relations at small degrees of melting, but with higher degrees of melting this effect steadily decreases. The CMASF data are best suited to modeling of melt generation from depleted sources that still contain all the major lherzolite phases. At low degrees of melting, however, the melting relations in the CMASF system deviate strongly from melting of natural mantle compositions.

ACKNOWLEDGEMENTS

We thank Paul Asimow, Glenn Gaetani, Michael Walter and Marjorie Wilson for very helpful journal reviews. Michael Walter provided help with computer programs and invaluable discussions, and Ping Shi kindly provided unpublished pyroxene compositions. This work was supported by National Science Foundation grants EAR-92191599 and EAR-9725900, and Texas Advanced Research Program grant 009741-046 to D.C.P. Part of the manuscript was prepared during the tenure of G.H.G. at the University of Bristol, where he was supported by NERC grant GR3/10120 to B. J. Wood, and at the Nordic Volcanological Institute, where G.H.G. is supported by NordVulk research fellowship. This paper is Contribution 896, Department of Geosciences, University of Texas at Dallas.

REFERENCES

Albee, A. L. & Ray, L. (1970). Correction factors for electron-probe microanalysis of silicates, oxides, carbonates, and sulphates. *Analytical Chemistry* **42**, 1408–1414.

Asimow, P. D., Hirschmann, M. M., Ghiorso, M. S., O'Hara, M. J. & Stolper, E. M. (1995). The effect of pressure-induced solid–solid phase transitions on decompression melting of the mantle. *Geochimica et Cosmochimica Acta* **59**, 4489–4506.

Asimow, P. D., Hirschmann, M. M. & Stolper, E. M (1997). An analysis of variations in isentropic melt productivity. *Philosophical Transactions of the Royal Society of London, Series A* **355**, 255–281.

Baker, M. B., Hirschmann, M. M., Ghiorso, M. S. & Stolper, E. M. (1995). Compositions of near-solidus peridotite melts from experiments and thermodynamic calculations. *Nature* **375**, 308–311.

Ballhaus, C. & Frost, B. R. (1994). The generation of oxidized CO_2-bearing basaltic melts from reduced CH_4-bearing upper mantle sources. *Geochimica et Cosmochimica Acta* **58**, 4931–4940.

Basaltic Volcanism Study Project (1981). *Basaltic Volcanism on the Terrestrial Planets*. New York: Pergamon Press.

Bertka, C. M. & Holloway, J. R. (1993). Pigeonite at solidus temperatures: implications for partial melting. *Journal of Geophysical Research* **98**, 19755–19766.

Bowen, N. L. & Schairer, J. F. (1935). The system MgO–FeO–SiO_2. *American Journal of Science* **29**, 151–217.

Bryndzia, L. T., Wood, B. J. & Dick, H. J. B. (1989). The oxidation state of the Earth's sub-oceanic mantle from oxygen thermobarometry of abyssal spinel peridotites. *Nature* **341**, 526–527.

Carter, J. L. (1970). Mineralogy and chemistry of the Earth's upper mantle based on the partial fusion–partial crystallization model. *Geological Society of America Bulletin* **81**, 2021–2034.

Christie, D. M., Carmichael, I. S. E. & Langmuir, C. H. (1986). Oxidation states of mid-ocean ridge basalt glasses. *Earth and Planetary Science Letters* **79**, 397–411.

Davis, B. T. C. (1964). The system diopside–forsterite–pyrope at 40 kilobars. *Carnegie Institution of Washington Yearbook* **63**, 165–171.

Davis, B. C. T. & Schairer, J. F. (1965). Melting relations in the join diopside–forsterite–pyrope at 40 kilobars and at one atmosphere. *Carnegie Institution of Washington Yearbook* **64**, 123–126.

Dick, H. J. B. & Fisher, R. L. (1984). Mineralogic studies of the residues of mantle melting: abyssal and alpine-type peridotites. In: Kornprobst, J. (ed.) *Kimberlites II: The Mantle and Crust–Mantle Relationships*. Amsterdam: Elsevier, pp. 295–308.

Dick, H. J. B., Fisher, R. L. & Bryan, W. B. (1984). Mineralogic variability of the uppermost mantle along mid-ocean ridges. *Earth and Planetary Science Letters* **69**, 88–106.

Fujii, T., Tachikara, M. & Kurita, K. (1989). Melting experiments in the system CaO–MgO–Al_2O_3–SiO_2 to 8 GPa: constraints on the origin of komatiites. *EOS Transactions, American Geophysical Union* **70**, 483.

Grover, J. E., Lindsley, D. H. & Bence, A. E. (1980). Experimental phase relations of olivine vitrophyres from breccia 14321: the temperature- and pressure-dependence of Fe–Mg partitioning for olivine and liquid in highland melt-rocks. *Proceedings of the 11th Lunar and Planetary Science Conference*, 179–196.

Gudfinnsson, G. H. & Presnall, D. C. (1996). Melting relations of model lherzolite in the system CaO–MgO–Al_2O_3–SiO_2 at 2·4–3·4 GPa and the generation of komatiites. *Journal of Geophysical Research* **101**, 27701–27709.

Hart, S. R. & Zindler, A. (1986). In search of a bulk-earth composition. *Chemical Geology* **57**, 247–267.

Heinrich, K. F. J. (1986). Comparisons of algorithms for X-ray mass absorption coefficients. *Microbeam Analysis* **21**, 279–280.

Herzberg, C. & Gasparik, T. (1991). Garnet and pyroxenes in the mantle: a test of the majorite fractionation hypothesis. *Journal of Geophysical Research* **96**, 16263–16274.

Herzberg, C., Gasparik, T. & Sawamoto, H. (1990). Origin of mantle peridotite: constraints from melting experiments to 16·5 GPa. *Journal of Geophysical Research* **95**, 15779–15803.

Hirschmann, M. M., Stolper, E. M. & Ghiorso, M. S. (1994). Perspectives on shallow mantle melting from thermodynamic calculations. *Mineralogical Magazine* **58**, 418–419.

Hirschmann, M. M., Baker, M. B. and Stolper, E. M. (1998). The effect of alkalies on the silica content of mantle-derived magmas. *Geochimica et Cosmochimica Acta* **62**, 883–902.

Jaques, A. L. & Green, D. H. (1980). Anhydrous melting of peridotite at 0–15 kb pressure and the genesis of tholeiitic basalts. *Contributions to Mineralogy and Petrology* **73**, 287–310.

Johnson, K. T. M., Dick, H. J. B. & Shimizu, N. (1990). Melting in the oceanic upper mantle: an ion microprobe study of diopsides in abyssal peridotites. *Journal of Geophysical Research* **95**, 2661–2678.

Kinzler, R. J. & Grove, T. L. (1992*a*). Primary magmas of mid-ocean ridge basalts, 1. Experiments and methods. *Journal of Geophysical Research* **97**, 6885–6906.

Kinzler, R. J. & Grove, T. L. (1992*b*). Primary magmas of mid-ocean ridge basalts, 2. Applications. *Journal of Geophysical Research* **97**, 6907–6926.

Kinzler, R. J. & Grove, T. L. (1993). Corrections and further discussion of the primary magmas of mid-ocean ridge basalts, 1 and 2. *Journal of Geophysical Research* **98**, 22339–22347.

Klein, E. M. & Langmuir, C. H. (1987). Global correlations of ocean ridge basalt chemistry with axial depth and crustal thickness. *Journal of Geophysical Research* **92**, 8089–8115.

Korzhinskii, D. S. (1959). *Physicochemical Basis of the Analysis of the Paragenesis of Minerals*. New York: Consultants Bureau.

Kushiro, I. (1979). Fractional crystallization of basaltic magma. In: Yoder, H. S., Jr (ed.) *The Evolution of the Igneous Rocks: Fiftieth Anniversary Perspectives*. Princeton, NJ: Princeton University Press, pp. 171–203.

Kushiro, I. & Walter, M. J. (1998). Mg–Fe partitioning between olivine and mafic–ultramafic melts. *Geophysical Research Letters* **25**, 2337–2340.

Langmuir, C. H., Klein, E. M. & Plank, T. (1992). Petrological systematics of mid-ocean ridge basalts: constraints on melt generation beneath ocean ridges. In: Phipps Morgan, J., Blackman, D. K. & Sinton, J. M. (eds) *Mantle Flow and Melt Generation at Mid-Ocean Ridges. Geophysical Monograph, American Geophysical Union* **71**, 183–280.

Lindsley, D. H. (1983). Pyroxene thermometry. *American Mineralogist* **68**, 477–493.

Liu, L.-G. & Bassett, W. A. (1975). The melting of iron up to 200 kbar. *Journal of Geophysical Research* **80**, 3777–3782.

Liu, T.-C. & Presnall, D. C. (1990). Liquidus phase relationships on the join anorthite–forsterite–quartz at 20 kbar with applications to basalt petrogenesis and igneous sapphirine. *Contributions to Mineralogy and Petrology* **104**, 735–742.

Liu, T.-C. & Presnall, D. C. (2000). Liquidus phase relations in the system CaO–MgO–Al_2O_3–SiO_2 at 2·0 GPa: applications to basalt fractionation, eclogites, and igneous sapphirine. *Journal of Petrology* **41**, 3–20.

Longhi, J. & Bertka, C. M. (1996). Graphical analysis of pigeonite–augite liquidus equilibria. *American Mineralogist* **81**, 685–695.

McDonough, W. F. & Sun, S.-S. (1995). The composition of the Earth. *Chemical Geology* **120**, 223–253.

McKenzie, D. & Bickle, M. J. (1988). The volume and composition of melt generated by extension of the lithosphere. *Journal of Petrology* **29**, 625–679.

Milholland, C. S. & Presnall, D. C. (1998). Liquidus phase relations in the CaO–MgO–Al_2O_3–SiO_2 system at 3·0 GPa: the aluminous pyroxene thermal divide and high-pressure fractionation of picritic and komatiitic magmas. *Journal of Petrology* **39**, 3–27.

Morse, S. A. (1980). *Basalts and Phase Diagrams*. New York: Springer.

Mysen, B. O. & Kushiro, I. (1977). Compositional variations of coexisting phases with degree of melting of peridotite in the upper mantle. *American Mineralogist* **62**, 843–865.

Mysen, B. O., Virgo, D. & Seifert, F. A. (1982). The structure of silicate melts: implications for chemical and physical properties of natural magma. *Reviews of Geophysics* **20**, 353–383.

Niu, Y. & Batiza, R. (1991). An empirical method for calculating melt compositions produced beneath mid-ocean ridges: application for axis and off-axis (seamounts) melting. *Journal of Geophysical Research* **96**, 21753–21777.

O'Hara, M. J. & Yoder, H. S. (1967). Formation and fractionation of basic magmas at high pressures. *Scottish Journal of Geology* **3**, 67–117.

Presnall, D. C. (1964). Deduction of liquid crystallization paths in a five-component oxide system containing iron. *Carnegie Institution of Washington Yearbook* **63**, 133–135.

Presnall, D. C. (1969). The geometrical analysis of partial fusion. *American Journal of Science* **267**, 1178–1194.

Presnall, D. C. (1976). Alumina content of enstatite as a geobarometer for plagioclase and spinel lherzolites. *American Mineralogist* **61**, 582–588.

Presnall, D. C. (1986). An algebraic method for determining equilibrium crystallization and fusion paths in multicomponent systems. *American Mineralogist* **71**, 1061–1070.

Presnall, D. C. (1991). Algebraic methods for determining directions of decreasing temperature along isobaric liquidus univariant lines. *Canadian Mineralogist* **92**, 687–692.

Presnall, D. C., Brenner, N. L. & O'Donnell, T. H. (1973). Drift of Pt/Pt10Rh and W3Re/W25Re thermocouples in single stage piston-cylinder apparatus. *American Mineralogist* **58**, 771–777.

Presnall, D. C., Dixon, S. A., Dixon, J. R., O'Donnell, T. H., Brenner, N. L., Schrock, R. L. & Dycus, D. W. (1978). Liquidus phase relations on the join diopside–forsterite–anorthite from 1 atm to 20 kbar: their bearing on the generation and crystallization of basaltic magma. *Contributions to Mineralogy and Petrology* **66**, 203–220.

Presnall, D. C., Dixon, J. R., O'Donnell, T. H. & Dixon, S. A. (1979). Generation of mid-ocean ridge tholeiites. *Journal of Petrology* **20**, 3–35.

Preston-Thomas, H. (1990). The International Temperature Scale of 1990 (ITS-90). *Metrologia* **27**, 3–10, 107.

Ringwood, A. E. (1975). *Composition and Petrology of the Earth's Mantle*. New York: McGraw–Hill.

Roeder, P. L. & Emslie, R. F. (1970). Olivine–liquid equilibrium. *Contributions to Mineralogy and Petrology* **29**, 275–289.

Sen, G. & Presnall, D. C. (1984). Liquidus phase relationships on the join anorthite–forsterite–quartz at 10 kbar with applications to basalt petrogenesis. *Contributions to Mineralogy and Petrology* **85**, 404–408.

Shi, P. & Libourel, G. (1991). The effects of FeO on the system CMAS at low pressure and implications for basalt crystallization processes. *Contributions to Mineralogy and Petrology* **108**, 129–145.

Takahashi, E. & Irvine, T. N. (1981). Stoichimetric control of crystal/liquid single-component partition coefficients. *Geochimica et Cosmochimica Acta* **45**, 1181–1185.

Takahashi, E. & Kushiro, I. (1983). Melting of dry peridotite at high pressures and magma genesis. *American Mineralogist* **68**, 859–879.

Ulmer, P. (1989). The dependence of the Fe^{2+}–Mg cation partitioning between olivine and basaltic liquid on pressure, temperature and composition. *Contributions to Mineralogy and Petrology* **101**, 261–273.

Walter, M. J. (1998). Melting of garnet peridotite and the origin of komatiite and depleted lithosphere. *Journal of Petrology* **39**, 26–60.

Walter, M. J. & Presnall, D. C. (1994). Melting behaviour of simplified lherzolite in the system CaO–MgO–Al_2O_3–SiO_2–Na_2O from 7 to 35 kbar. *Journal of Petrology* **35**, 329–359.

Walter, M. J., Sisson, T. W. & Presnall, D. C. (1995). A mass proportion method for calculating melting reactions and application to melting of model upper mantle lherzolite. *Earth and Planetary Science Letters* **135**, 77–90.